



저작자표시-비영리-변경금지 2.0 대한민국

이용자는 아래의 조건을 따르는 경우에 한하여 자유롭게

- 이 저작물을 복제, 배포, 전송, 전시, 공연 및 방송할 수 있습니다.

다음과 같은 조건을 따라야 합니다:



저작자표시. 귀하는 원저작자를 표시하여야 합니다.



비영리. 귀하는 이 저작물을 영리 목적으로 이용할 수 없습니다.



변경금지. 귀하는 이 저작물을 개작, 변형 또는 가공할 수 없습니다.

- 귀하는, 이 저작물의 재이용이나 배포의 경우, 이 저작물에 적용된 이용허락조건을 명확하게 나타내어야 합니다.
- 저작권자로부터 별도의 허가를 받으면 이러한 조건들은 적용되지 않습니다.

저작권법에 따른 이용자의 권리는 위의 내용에 의하여 영향을 받지 않습니다.

이것은 [이용허락규약\(Legal Code\)](#)을 이해하기 쉽게 요약한 것입니다.

[Disclaimer](#)

이학박사 학위논문

Growth and Characterization of
Position Controlled
Droplet Epitaxy Quantum Dots

금속방울 성장법을 이용한
위치 선정 양자점의 성장과 분석

2018 년 8 월

서울대학교 대학원
물리천문학부
박 석 인

Doctoral Thesis

Growth and Characterization of
Position Controlled
Droplet Epitaxy Quantum Dots

August 2018

Department of Physics and Astronomy
Seoul National University

Suk In Park

Growth and Characterization of Position Controlled Droplet Epitaxy Quantum Dots

금속방울 성장법을 이용한
위치 선정 양자점의 성장과 분석

지도교수 이 규 철

이 논문을 이학박사 학위논문으로 제출함
2018 년 8 월

서울대학교 대학원
물리 · 천문학부
박 석 인

박석인의 박사학위논문을 인준함
2018 년 8 월

위 원 장 이 탁 희 (인)

부 위 원 장 이 규 철 (인)

위 원 홍 승 훈 (인)

위 원 박 윤 (인)

위 원 송 진 동 (인)

Abstract

Growth and Characterization of Position Controlled Droplet Epitaxy Quantum Dots

Suk In Park

Department of Physics and Astronomy

The Graduate School

Seoul National University

Semiconductor quantum dots have been studied extensively for various quantum optical devices. Recently, it has been demonstrated that single quantum dots have the potential to be used in quantum cryptography and quantum computing. However, in order to realize a practical quantum device for such applications, many obstacles remain. Droplet epitaxy is a versatile method in the growth of quantum nanostructures. The separation of group III materials and group V materials has opened up new possibilities in the growth of nanostructures. By using droplet epitaxy, it is possible to overcome the obstacles which

have been associated with conventional self assembled quantum dot growth for quantum optic devices such as single photon emitters.

In this thesis, droplet epitaxy and growth methods derived from droplet epitaxy has been researched for the use quantum optic device applications. The basic growth technique for Ga droplets were experimented with various arsenization processes. An annealing method which improves the optical quality of the quantum dots under a thin capping layer for the use of surface plasmonics was developed with droplet epitaxial quantum dots.

Among the many uses of metal droplets, an in-situ etching method was studied and used for improved quantum dots. The nanoholes generated by the droplet drilling were used as a template for symmetric quantum dots. Shape symmetry of the quantum dots is an important factor in generating entangled photon pairs, which is used for quantum information devices. The nanoholes were filled with InAs to form In(Ga)As quantum dots. A multistage drilling method was developed to overcome temperature limitations of the droplet drilling process. The multistage drilling method was also utilized for the position control of the quantum dots by combining it with an AFM lithography method. The results show promising characteristics for quantum optic device applications.

Table of contents

| | |
|--|-----------|
| Chapter 1. Introduction..... | 1 |
| 1-1 Quantum dots..... | 1 |
| 1-2 Molecular beam epitaxy | 5 |
| 1-3 MBE growth basics | 8 |
| 1-4 Self assembled quantum dots | 13 |
| Reference | 14 |
| | |
| Chapter 2. Experiment | 15 |
| 2-1 Molecular beam epitaxy system | 15 |
| 2-2 Structural measurement | 17 |
| 2-3 Optical characterization..... | 20 |
| Reference | 22 |
| | |
| Chapter 3. Growth of quantum dots | 23 |
| 3-1 Droplet epitaxy | 23 |
| 3-2 Internal thermal heating..... | 33 |
| 3-3 Droplet drilled holes | 40 |

| | |
|---|------------|
| 3-4 Additional drilling of holes and InAs filling | 51 |
| 3-5 Summary..... | 60 |
| Reference | 62 |
| Chapter 4. Optical characterization of quantum dots..... | 63 |
| 4-1 Photoluminescence of a quantum dot..... | 63 |
| 4-2 Photoluminescence of hole filled quantum dot | 71 |
| 4-3 Symmetry of quantum dots | 74 |
| 4-4 Summary..... | 83 |
| Reference | 84 |
| Chapter 5. Site controlled quantum dots..... | 86 |
| 5-1 Local oxidation lithography by AFM | 86 |
| 5-2 Local oxidation etch with droplet drilling | 92 |
| Reference | 95 |
| Chapter 6. Conclusion | 98 |
| Abstract in Korean (국문 요약) | 100 |

List of Figures

| | |
|--|----|
| Figure 1-1 Schematic diagram of density of states in 3,2,1 and 0 dimensional hetero structures [1]. | 2 |
| Figure 1-2 The confinement energy in a spherical GaAs quantum dot surrounded by a Ga _{0.8} Al _{0.2} As barrier [4] | 4 |
| Figure 1-3 Isosurface plots of the total probability densities(a,b) and valence-band projections (c)-(e) of bound electron and hole state in a pyramidal InAs/GaAs QD with base length of 11.3nm [2] | 5 |
| Figure 1-4 Schematic representation of the processes occurring during epitaxial growth [5]. | 9 |
| Figure 1-5 Atomic-scale view of growth processes at surface [6]. | 10 |
| Figure 1-6 Balance of surface free energy for an island deposited on a substrate [7] | 11 |
| Figure 1-7 Schematic of a) Volmer-Weber, b) Frank-Van der Merwe, and c) Stranski-Krastanov growth modes. | 12 |
| Figure 2-1 Cluster of MBE in KIST[1] | 15 |
| Figure 2-2 A schematic of the MBE at KIST[1] | 16 |

| | |
|---|----|
| Figure 2-3 InP absorption edge shift at various temperatures used for BandiT[2] | 17 |
| | 17 |
| Figure 2-4 Schematic of atomic force microscope (AFM)..... | 18 |
| Figure 2-5 SEM image of the tip of an AFM cantilever[3] | 19 |
| Figure 2-5 Micro photoluminescence setup at KIST..... | 21 |
| Figure 3-1 RHEED intensity for Ga deposition and As irradiation [1] | 24 |
| Figure 3-2 Surface density N of GaAs QDs [2]..... | 25 |
| Figure 3-3 Temperature dependence of droplet density..... | 27 |
| Figure 3-4 Flux dependence of droplet diameter..... | 29 |
| Figure 3-5 Schematic of kinetic processes that determine nanostructural development [5]..... | 31 |
| Figure 3-6 AFM images of different nanostructures in the droplet arsenization process[4]..... | 32 |
| Figure 3-7 a) GaAs droplet QDs growth procedure with an internal thermal heating step b) Dimensions (width and height), c) aspect ratio (height/width) and d) density of the QDs with no ITH and as a function of ITH temperature | 36 |
| Figure 3-8 (a) Schematic of the droplet QDs (b) SEM of droplet QDs (c) wide range AFM showing the density of the QDs. (d) AFM image of a single QD..... | 37 |

Figure 3-9 a) Photoluminescence image showing the emission of several QDs, collected under 455 nm LED illumination. b) Photoluminescence spectrum collected under 405 nm continuous-wave laser excitation with power density of $1.8 \times 10^{-4} \mu\text{W } \mu\text{m}^{-2}$, at a temperature of 4.7K. c) Emission intensity plotted as a function of laser excitation power for the emission line at 730.5 nm shown in b. ...39

Figure 3-10 Scheme of the droplet geometry and the processes considered in the core-shell model. [17].....41

Figure 3-11 Calculated and measured temperature dependence of (a) the critical time t_c up to hole formation, (b) the hole depth d_H , and (c) the wall height h_W . [17].....44

Figure 3-12 AFM image of a droplet drilled hole and the symmetry along perpendicular axes.46

Figure 3-13 TEM image of a droplet drilled hole. The interface is highlighted by a single layer of phosphorus.47

Figure 3-14 Basic growth process of a droplet drilled hole.....48

Figure 3-15 AFM images of a) Ga droplets, b) Ga droplets raised to the anneal temperature and cooled, and c) Ga droplets annealed for 10 minutes.....49

Figure 3-16 AFM images of Ga droplets with a) no annealing, b) 443°C anneal, c) 460°C anneal, and d) 480°C anneal50

| | |
|--|----|
| Figure 3-17 AFM image of a pit formed during annealing process of droplet drilling | 52 |
| Figure 3-18 Growth sequence of the multistage drilling process. | 53 |
| Figure 3-19 Multistage drilling with additional drilling at temperatures of a) 336°C b)362°C and c)386°C..... | 54 |
| Figure 3-20 AFM image of GaAs surfaces after a) initial drilling and after b)one, c)three, and d)six additional drillings | 55 |
| Figure 3-21 Density of holes(QDs) and depth dependence for additional drilling. | 56 |
| Figure 3-22 Symmetry of multistage drilled hole..... | 56 |
| Figure 3-23 AFM image drilled hole surface with an InAs coverage of a) 0.85 ML, b) 1.07 ML, c)1.31 ML, and d) 1.70 ML..... | 57 |
| Figure 3-24 Growth sequence of droplet drilled holes filled with InAs QDs. | 58 |
| Figure 3-25 AFM image of each step in the growth sequence of InAs filled nanohole QD..... | 59 |
| Figure 4-1 Schematic representation of energy levels in a quantum dot (QD) with two shells for carriers in the conduction and valence band, respectively. [1] | |

| | |
|---|----|
| | 65 |
| Figure 4-2 Diagram of the atomic four-level laser system. With the pump rate P an electron is excited from the ground state $ 1\rangle$ into the pump level $ 4\rangle$. [1] | 66 |
| Figure 4-3 QD model with carrier excitation in the p shells and recombination in the s shells..... | 67 |
| Figure 4-4 Schematic level diagram of possible electron and hole occupations for the s-shell of a quantum dot..... | 67 |
| Figure 4-5 Energy level scheme for the excitonic QD ground state without ($H^_A=0$) and with ($H^_A \neq 0$) inclusion of exchange interaction between electron and hole spins.[4]..... | 69 |
| Figure 4-6 Schematic of a) Non-resonant, b) quasi-resonant, and c) resonant optical excitation | 70 |
| Figure 4-7 a) Macro and b) micro photoluminescence of InGaAs filled nanoholes. | 72 |
| Figure 4-8 SEM image an 100nm thick gold layer with holes deposited on InAs filled hole quantum dot with a GaAs capping layer..... | 73 |
| Figure 4-9 a) Schematic of radiative decay process of the biexciton. b) The same two photon emission process in a simple energy level diagram. [1] | 75 |
| Figure 4-10 Biexciton–exciton cascade for a quantum dot with zero fine-structure | |

splitting (left) and non-zero fine-structure splitting (right). The top row depicts the energy level schemes and below the corresponding emission spectra are depicted.

[6].....76

Figure 4-11 (a) Macro-PL spectra at 2 K measured for the [110] (thick curve) and [110] (thin curve) polarizations; (b) Degree of linear polarization of PL spectra shown in (a). The PL band from the GaAs observed at 1.5 eV is isotropic, while those from the InP SADs (1.63 eV) and Ga_{0.5}In_{0.5}P (1.87 eV) show strong optical anisotropy; (c) Polarization dependence of macro-PL spectra measured using another sample with a different degree of matrix ordering. Since the InP SADs layer of sample 2 was grown at the same temperature as that of sample 1, the average dot sizes are the same between the both samples; (d) Degree of polarization of the PL spectra shown in (c) [14]78

Figure 4-12 Schematic of the optical setup to measure the polarity of quantum dots.80

Figure 4-13 Linear polarization dependence of the exciton X at various electric fields [15].....81

Figure 4-14 Polarization measurement for QDs with InAs coverage of a) 0.63 ML, b) 0.85 ML c) 1.07 ML and d) 1.07ML with DBR.82

| | |
|---|----|
| Figure 5-1 Site-controlling methods reported by various groups. a)[15], b)[16], c)[17]..... | 87 |
| Figure 5-2 Schematic of an anodic oxidation lithography..... | 88 |
| Figure 5-3 a) The growth rate vs. electric field strength. b) Growth rate vs. oxide height at three tip biases [20]..... | 89 |
| Figure 5-4 AFM image of a) oxidation and b) etched holes. Exposure time dependence of c) height of a) and depth of b) and d) diameter | 90 |
| Figure 5-5 AFM image of etched oxide mounds [a,b)] and the cross section scan for perpendicular directions | 91 |
| Figure 5-6 Schematic of the local oxidation pattern combined with droplet drilling. | 93 |
| Figure 5-7 AFM images of droplet drilled holes before and after being filled with Ga droplets..... | 94 |

1. Introduction

1-1 Quantum dots

Quantum dots (QD) are tiny semiconductor particles which have optical and electronic properties that differ from bulk material. They are referred to as “artificial atoms” due to their discrete electronic states. Their optoelectronic properties change as a function of both size and shape. Larger QDs emit longer wavelength while smaller QDs emit shorter wavelength, thus the color of the light emitted by the QDs are highly tunable. Thus QDs have attracted great interest for potential applications in solar cells, LEDs, laser diodes and quantum computing.

Quantum confinement for various dimensions is illustrated in Figure 1-1. The distribution of energy levels in quantum structures is varied by the dimension of the nanostructure. Figure 1-1 shows the variation of the density of state in structures of various dimensionality.

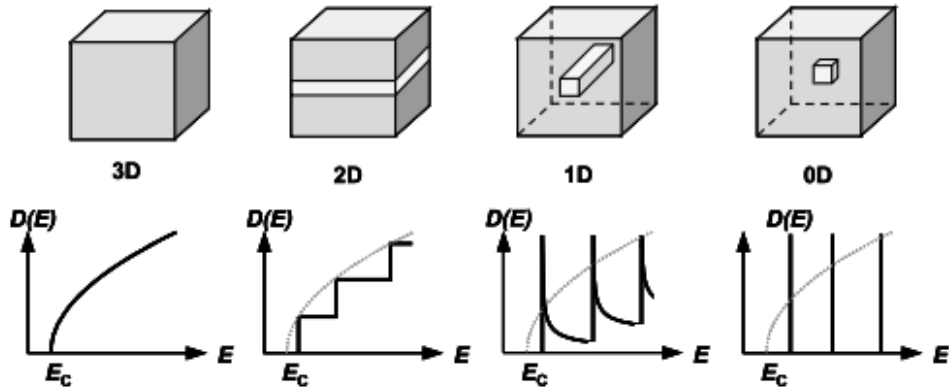


Figure 1-1 Schematic diagram of density of states in 3,2,1 and 0 dimensional hetero structures [1].

The density of states (DOS) for various dimensions is given by [2]

$$D_{3D}(E) = \frac{V}{2\pi} \left(\frac{2m^*}{\hbar} \right)^{3/2} \sqrt{E - E_n}$$

$$D_{2D}(E) = \frac{A m^*}{\pi \hbar^2} (E - E_n)$$

$$D_{1D}(E) = \frac{L}{\pi} \left(\frac{2m^*}{\hbar} \right)^{1/2} \frac{1}{\sqrt{E - E_n}}$$

$$D_{0D}(E) = 2\delta(E - E_n)$$

The δ -function like DOS at E_n for QDs suggests a high quantum efficiency suggesting it to be an excellent candidate for opto-electronic devices. [3] Such characteristics of the

QD lead to lower threshold current, higher differential gain and higher temperature operation in optoelectronic devices.

The size of the QDs also affects the energy states in QD. The energy states for a simple rectangular QD is given by

$$E_n = \frac{\hbar^2 \pi^2}{2m} \left[\left(\frac{n_x}{L_x} \right)^2 + \left(\frac{n_y}{L_y} \right)^2 + \left(\frac{n_z}{L_z} \right)^2 \right]$$

It can be seen as the size of the QD decrease the quantum confinement energy increase. This is also shown in Figure 1-2 where the energy levels are calculated confinement for a spherical quantum dot. The higher quantum confinement energy leads to a higher emission energy in optical properties.

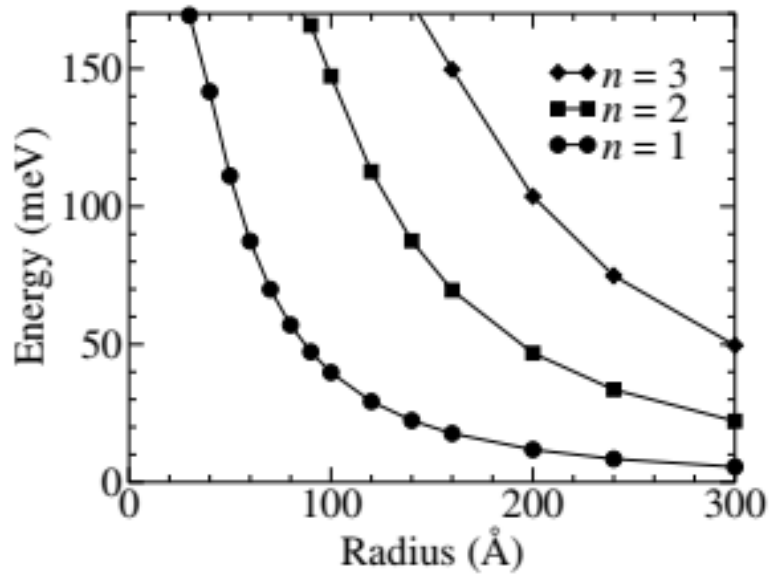


Figure 1-2 The confinement energy in a spherical GaAs quantum dot surrounded by a Ga_{0.8}Al_{0.2}As barrier [4]

For more realistic semiconductor QDs that are grown on substrates, the shape of the QD is similar to a pyramid or a dome. Simulation of a pyramidal QD is shown in Figure 1-3. The lowest four electron and hole wavefunctions are shown. This shows that the heavy hole character is dominant for lower hole states.

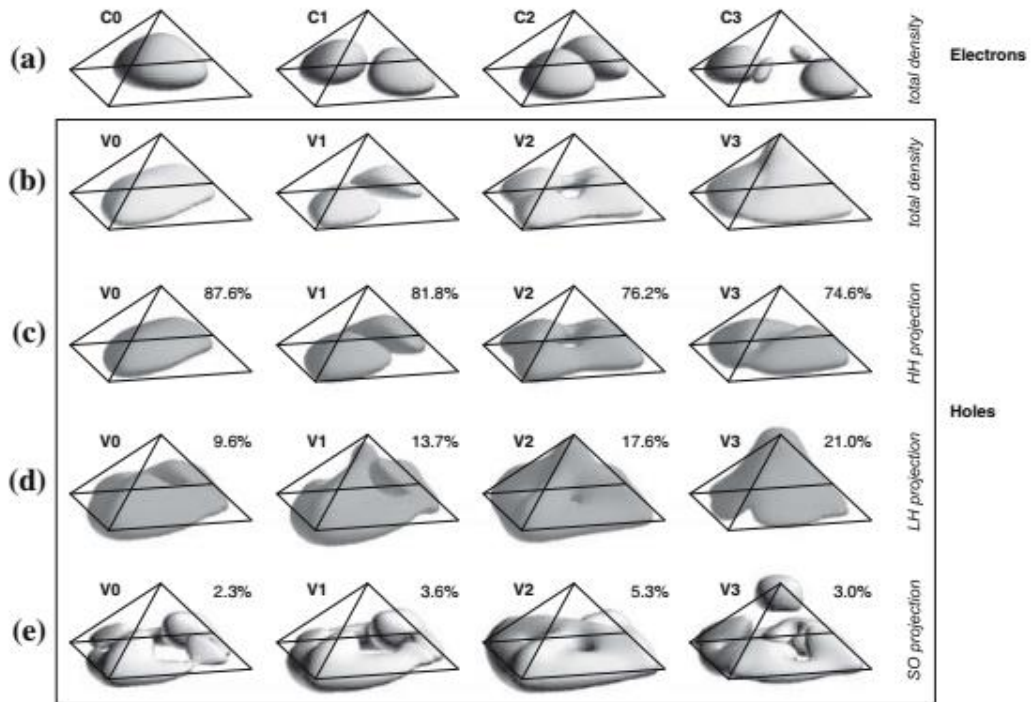


Figure 1-3 Isosurface plots of the total probability densities(a,b) and valence-band projections (c)-(e) of bound electron and hole state in a pyramidal InAs/GaAs QD with base length of 11.3nm [2]

1-2 Molecular beam epitaxy

The term epitaxy originates from the Greek words epi (επι), which means “above”, and taxis (τάξις), which means “in ordered manner”. It is normally translated as "arranging upon". For crystal growth, it means that deposited material form a crystalline overlayer that

has one well-defined orientation with respect to the substrate crystal structure (single-domain epitaxy). Molecular Beam Epitaxy (MBE), is a technique developed for growth of extremely high quality epitaxial thin layers on a substrate.

Since the invention in the late 1960s at Bell Labs, Molecular Beam Epitaxy has been widely used for research and manufacture of semiconductor devices. Among various growth methods, the most versatile technique for growing thin epitaxial structures made of semiconductors, metals or insulators is the MBE. Molecular or atomic beams of growth elements react at the surface of a substrate at certain growth temperature under ultrahigh vacuum (UHV) to form a thin film crystal. Fine control of the composition of the grown epilayer and its dopants is possible by controlling the evaporation rates of the growth elements. To ensure that surface migration of the impinging elements on the substrate, a low growth rate of 1ML/s is used for the growth. Thin films grown with this method has a smooth surface in the atomic level. The precise control of the beam fluxes and growth conditions to achieve a layer by layer growth at atomic levels makes the MBE unique compared to other growth methods. Additionally, in-situ characterization of the growth surface enables real-time feedback of the growth of the thin film, resulting in the fabrication of sophisticated device structures. For this reason, optical and electronic devices grown with the MBE technique show superior characteristics and performance compared to other growth techniques. Devices which have applications in military, civilian and consumer system have been develop with MBE, such as quantum well lasers, vertical-cavity surface

emitting lasers, quantum well infrared photodetectors, quantum cascade lasers, high electron mobility transistors, and heterojunction bipolar transistors.

Since the MBE works in UHV, vacuum conditions are critical in the growth of crystals. The vacuum condition has effect on the mean free path. The mean free path of a typical MBE is required to be around 30 cm, which is the distance between the source and the substrate. If the pressure of the chamber is not low enough the molecular beam may scatter on the residual gas species. Thus, the operating pressure of the MBE has to be below a certain limit to ensure that the mean free path is greater than the distance from the source to the substrate. For an atom traveling from the evaporator at a temperature T with a diameter σ under a pressure p , the mean free path is calculated to be

$$l = \frac{kT}{\sqrt{2}\pi\sigma^2 p}$$

The cross section diameter σ is typically 2-5Å, which results in a mean free path of few meters at a pressure of 10^{-5} torr.

Another reason for UHV is the purity of the material. The base pressure of the MBE chamber is required to be less than 10^{-9} torr. This is due to our preference of the growth speed of the crystal from the molecular beam overwhelming the growth rate from residual gas. The impinging rate J , where molecules are hitting the surface of the substrate per unit area in a unit time, is given by the formula

$$J = \frac{p}{\sqrt{2}\pi mkT}$$

under the conditions of partial pressure p and molar weight m , at a temperature of T . For pressures below 10^{-9} torr, we conclude that the growth from residual gas is in the order of 1 monolayer in 28 hours.

To ensure the UHV of the chamber, a stainless steel chamber with metal gaskets and an oil-free pumping (like cryogenic, titanium sublimation, ion and turbomolecular pumps) is used. A preparation chamber to load and degas the substrates without breaking the vacuum of the growth chamber is also required. A long bake-out after the venting of the main chamber is critical during the maintenance of the MBE. A cryo-shroud filled with liquid nitrogen also reduces the evaporation from internal surfaces.

1-3 MBE growth basics

Understanding the growth process of the thin film and the underlying principles is important to explain the structure and morphology of a crystal structure and the interface of the substrate. Figure 1-4 illustrates the individual atomic processes which determine film growth in its initial stages.

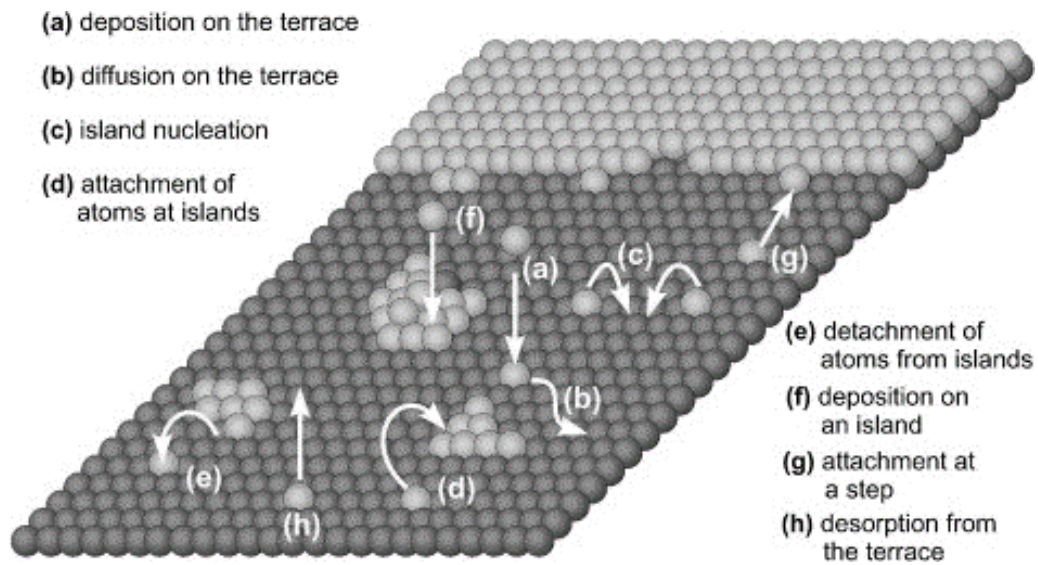


Figure 1-4 Schematic representation of the processes occurring during epitaxial growth [5].

Condensation of material from the molecular beam can be described by an impinging rate described in section 1-2. The condensed particle may immediately re-evaporate leaving the growth surface or it may diffuse along the surface, moving to various growth sites. At these growth sites such as edges or defects the diffused material may attach or it may re-evaporate. Additionally, when two or more atoms meet, a nucleus of an island is formed, where an two dimensional island is grown by attachment of additional adatoms or decay from desorption of atoms. Two dimensional islands are stable when the nuclei becomes larger than a critical nucleus, where the probability of growth and decay are equal. Direct impingement on two-dimensional islands, the attachment at a step and the desorption of the atoms from the terrace also occur on the growth surface.

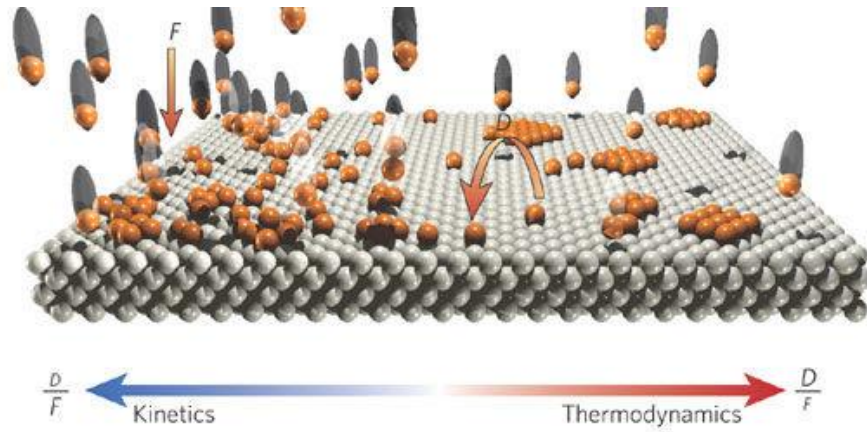


Figure 1-5 Atomic-scale view of growth processes at surface [6].

The ratio between the adatoms diffusion rate D and deposition flux F determines the type of growth. Figure 1-5 depict the thermodynamic and kinetic regime for different D/F ratios. At high D/F ratio thermodynamics is dominant resulting in film growth. At intermediate D/F ratios semiconductor nanostructures are usually grown.

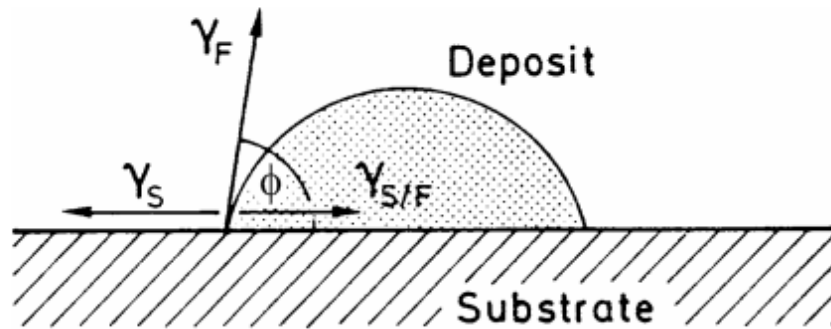


Figure 1-6 Balance of surface free energy for an island deposited on a substrate [7]

A simple model introduced by Bauer in 1958 describes three modes in crystal growth. Surface or interface energy γ , which is the free energy (per unit area) required to create an additional piece of surface or interface is used to determine the growth mode. γ is also known as the force per unit length of the boundary. As a result, equilibrium of the force at which the 3D island film and substrate meet can be described as

$$\gamma_S = \gamma_{S/F} + \gamma_F \cos \phi$$

where γ_S is the surface free energy of the substrate vacuum interface, γ_F that of the film–vacuum, and $\gamma_{S/F}$ that of the substrate–film interface. Comparing the free energy values when $\phi = 0$ determines the growth mode of the thin film. Layer-by-layer growth, also known as the Frank-van der Merve growth occurs when $\gamma_S \geq \gamma_{S/F} + \gamma_F$ when $\phi = 0$, while island growth, aka Volmer-Weber growth happens when $\gamma_S < \gamma_{S/F} + \gamma_F$. When a

slight lattice mismatch is present between the substrate and the thin film a third mode known as the layer-plus-island mode or Stranski-Krastanov(SK) mode occurs. In the SK growth mode, 3D islands grow on top of the first full layer. Layer to island growth transition occurs when the elastic strain field exceeds adhesion forces within the deposited material.

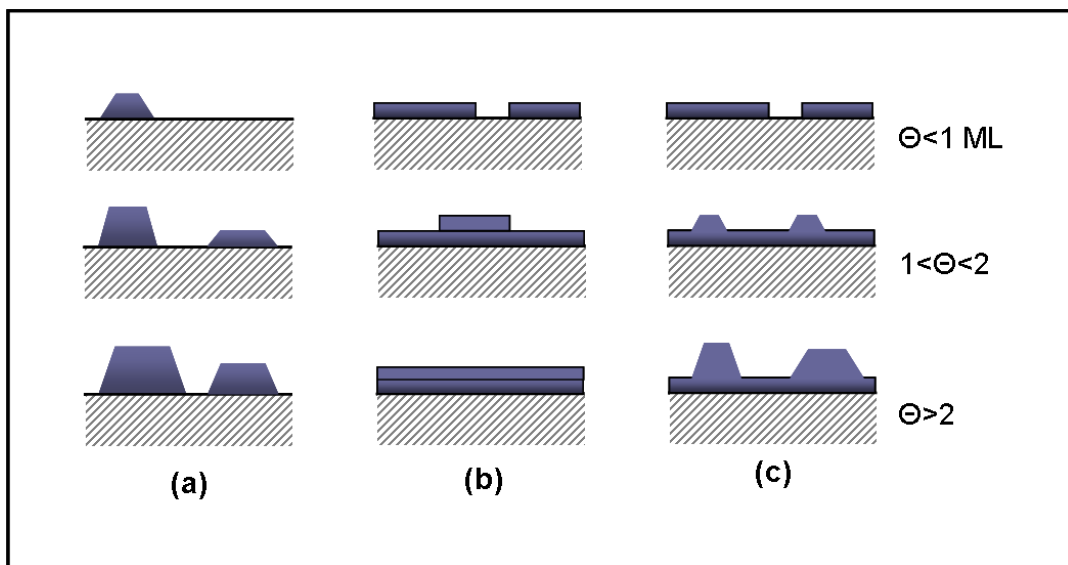


Figure 1-7 Schematic of a) Volmer-Weber, b) Frank-Van der Merwe, and c) Stranski-Krastanov growth modes

1-4 Self assembled quantum dots

Since the 1950s, experiments to study the size quantization effects were conducted by fabricating ultrathin layers and nanostructures. Fabrication of quantum dots was first developed in the early 1980s by etching a quantum well with lithography to leave islands. QDs were also grown on patterned substrates. By the mid 1980s, self assembly of quantum dots were being examined. A spontaneous formation occurs when lattice of the material is much larger than the substrate. When an InAs layer remains planar to a critical thickness three-dimensional islands form in a heteroepitaxy of InAs/GaAs. This is the Stranski-Krastanov growth mode we have discussed in the previous section. The lattice mismatch of 7.2% in the InAs/GaAs system causes islands to form on the surface of the strained InAs/GaAs superlattice. The InAs deposited on the substrate compresses to match the lattice of the GaAs substrate. The strain accumulates as the layers are stacked and after a certain threshold it becomes favorable for islands to form.

Reference

- [1] D. Bimberg, *Semiconductor Nanostructures*, Springer-Verlag Berlin Heidelberg, (2008)
- [2] M. Grundmann, *The Physics of Semiconductors*, Springer International Publishing, (2016)
- [3] Y. Masumoto, *Semiconductor Quantum Dots*, Springer-Verlag Berlin Heidelberg (2002)
- [4] P. Harrison, A. Valavanis, *Quantum Wells, Wires and Dots: Theoretical and Computational Physics of Semiconductor Nanostructures*, Fourth Edition, John Wiley & Sons, Ltd (2016)
- [5] B. Voigtländer *Surf. Sci. Rep.* 43, 127, (2001)
- [6] J.V. Barth et al., *Nature* 437, 671 (2005)
- [7] H. Luth, *Solid surfaces, interfaces and thin films*, Springer (2001)

2. Experiment

2-1 Molecular beam epitaxy system

The MBE system used in this work is a Riber Compact 21E produced by Riber Inc in France. Figure 2-1 shows a picture of the MBE cluster at KIST. Three MBE systems, an E-beam evaporator and a sputter system in clustered with tunnel chamber, which allows for sequential growth without exposure to air.

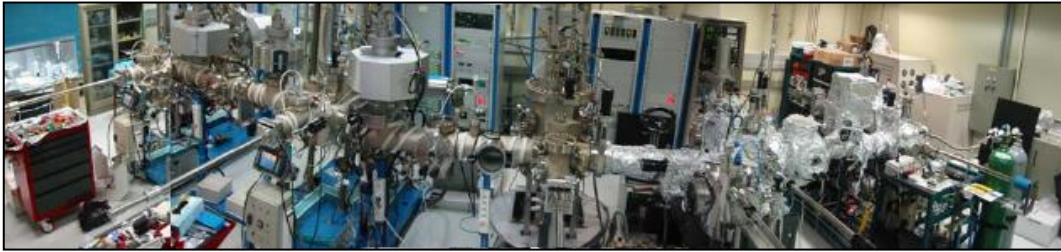


Figure 2-1 Cluster of MBE in KIST[1]

Figure 2-2 is a schematic of the MBE system mainly used for growth of quantum dots in this work. The MBE system includes 3 types of metal in group III (In, Ga, and Al) and 3 types of group V materials (P, As, and Sb). Si and Be are available for doping of n and p type semiconductors, respectively. A standard two zone Knudsen cell with a SUMO crucible is used for Ga and In to ensure large charge capacity and minimized long-term depletion effects with excellent flux uniformity. For aluminum, a standard K-cell with a conic crucible is used, due to its creeping nature. A backup Al cell is installed as insurance to the low volume of the conic crucible. For As and P sources, a standard valved cracker

cell is used to control the flux of the group V materials. The MBE is also equipped with a flux gauge, which is critical in reproduction of the metal growth rate on a daily basis. For in-situ monitoring of the crystal growth, a Reflection high-energy electron diffraction (RHEED) fluorescent screen combined with an electron gun is installed. Temperature measurement, which is one of the most critical factors in MBE growth is monitored by three methods. A C-type thermocouple is looped into a feedback cycle to control the substrate heater. A kSA BandiT, which uses the temperature-dependent optical absorption edge inherent in semiconductor materials, and a pyrometer redundantly monitors the substrate temperature. This redundancy of the surface temperature combined with the daily measurement of the flux allows for high reproducibility in MBE growth. UHV is maintained using an ion pump and cryo pump.

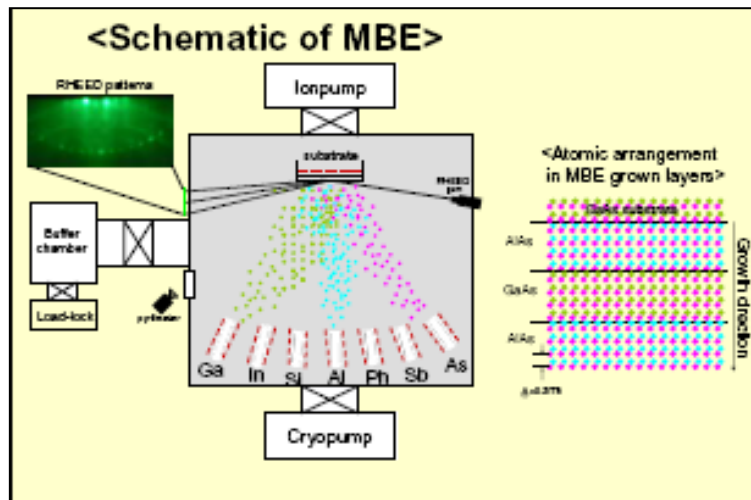


Figure 2-2 A schematic of the MBE at KIST[1]

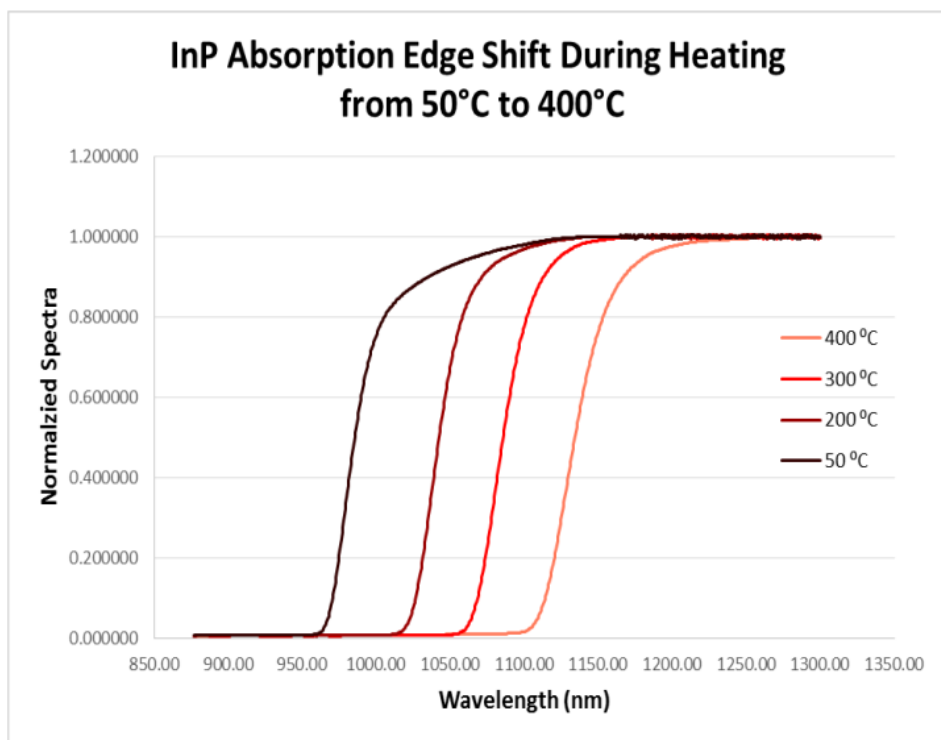


Figure 2-3 InP absorption edge shift at various temperatures used for BandiT[2]

2-2 Structural measurement

The structural measurement and surface morphology measurement are conducted using an atomic force microscope (AFM), scanning electron microscopy (SEM), and tunneling electron microscopy (TEM). Characterization of the surface morphology is a critical part of understanding quantum dots.

AFM measurement is a technique which relies on the van der Waals force between the tip of the cantilever and the surface of the sample. A nanoscale cantilever hovers above the surface of the sample. A laser beam reflects from the top of the cantilever and reaches the position sensitive photo detector (PSPD). Movement of the cantilever moves the position of the reflected laser on the PSPD, which is then fed into a feedback system to control the piezo scanner to keep the cantilever at a constant position. A Park Systems XE-100 AFM system was used for this work.

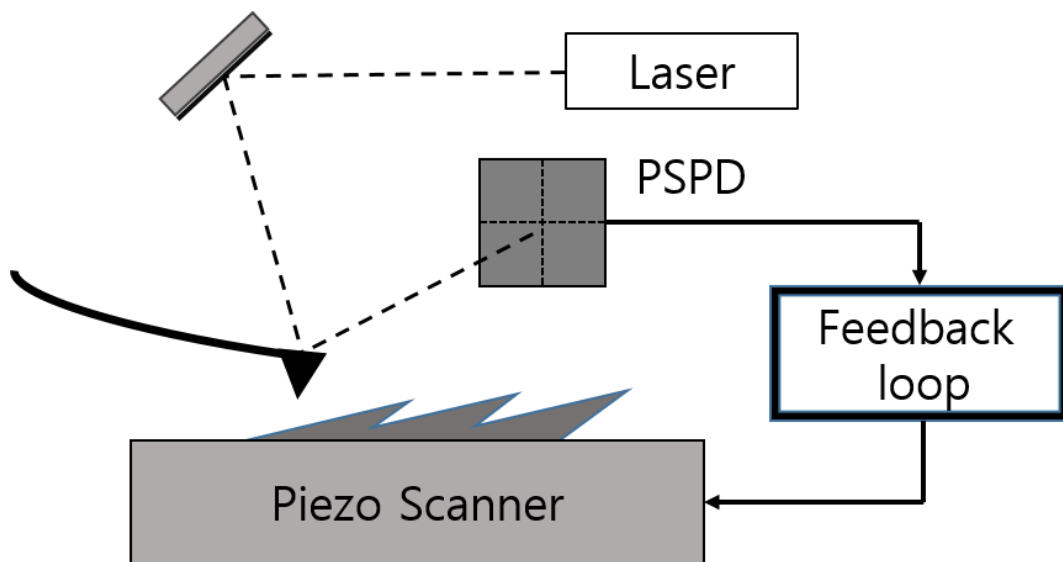


Figure 2-4 Schematic of atomic force microscope (AFM)

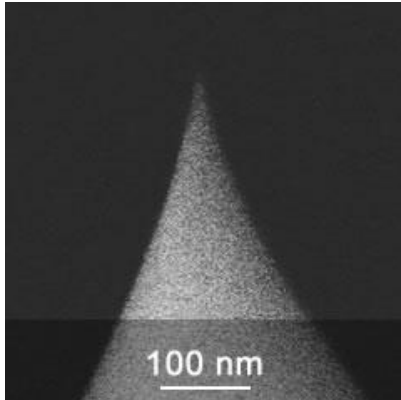


Figure 2-5 SEM image of the tip of an AFM cantilever[3]

A scanning electron microscope (SEM) is a type of electron microscope that produces images by scanning the surface of the sample with a focused beam of electrons. The electrons interact with the atoms of the sample to produce signals which are used to characterize the surface topography and composition. The detection of secondary electrons emitted by the electron beam is the most common mode used for SEM. By collecting the secondary electrons topography of the sample can be imaged.

TEM imaging is a powerful tool used to characterize crystal structures at the nanoscale level. An electron beam is transmitted through a sample to form an image. The sample is typically less than 100nm in thickness. Due to the small de Broglie wavelength of electrons crystallinity of the samples can be characterized in the atomic scale.

2-3 Optical characterization

Photoluminescence (PL) is light emission from any form of matter after the absorption of photons (electromagnetic radiation). PL occurs when electrons and holes in a semiconductor excited by a photoexcitation recombine to emit a photon. When a semiconductor absorbs photons with energy greater than its band gap, an electron is excited to the conduction band leaving a hole. Electrons and holes are attracted by Coulomb force and form a quasiparticle called excitons. Characterization of these excitons are crucial part of analyzing QDs.

A typical PL measurement setup uses a laser with a spot size of 100 μm . In order to analyze a single QD a micro PL setup is required. A photograph of the micro PL setup is shown in Figure 2-6. The small spot size of the laser combined with a mask deposited on a low density QD sample allows for the analysis of few if not a single QD.

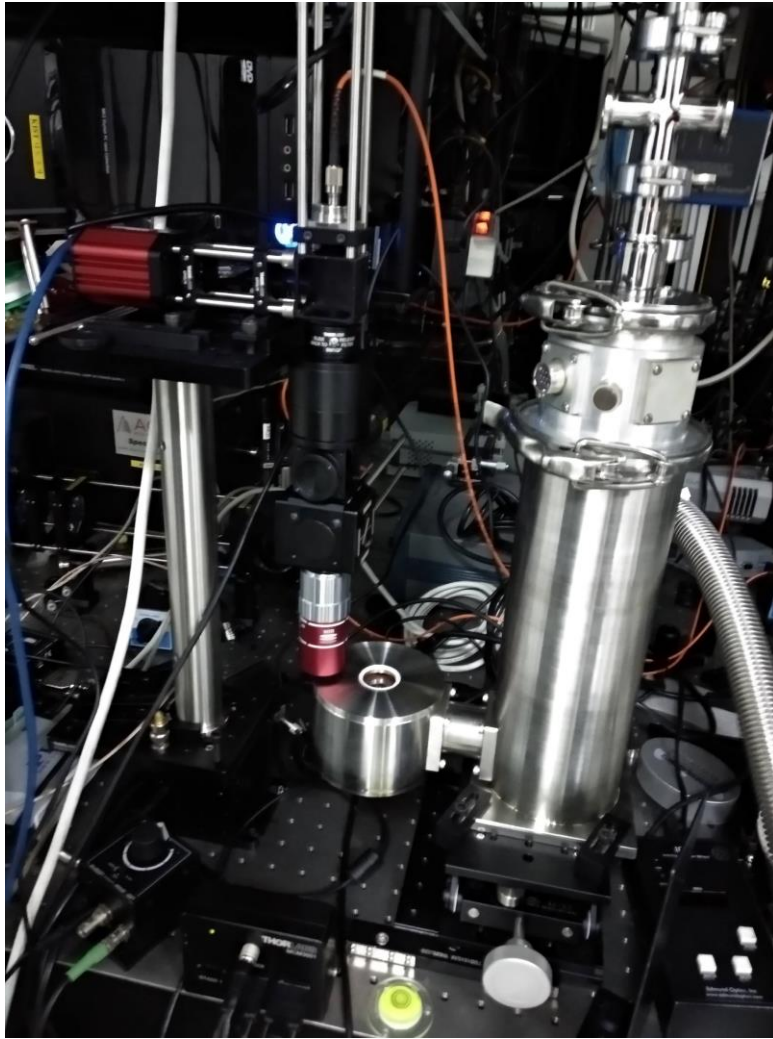


Figure 2-6 Micro photoluminescence setup at KIST

Reference

- [1] <http://imcm.kist.re.kr/?q=resource/cluster-mbe--molecular-beam-epitaxy-system>,
- [2] https://www.k-space.com/wp-content/uploads/BandiT_Product_Specs.pdf kSA
webpage
- [3] <https://www.spmtips.com/afm-tip-hq-nsc36-al-bs>

3. Growth of quantum dots

3-1 Droplet epitaxy

Koguchi and Ishige [1] first proposed the fabrication of GaAs microcrystals by droplet epitaxy in 1993. The concept of droplet epitaxy is to supply the two growth elements separately to form a nanostructure. This has the advantage of having elements such as In, Ga, Al to self-aggregate in nanoscale droplets, due to high surface tension. The group III droplets are then irradiated with group V elements to form a semiconductor nanostructure. Quantum dots fabricated by this method are buried in higher bandgap materials to exploit quantum confinement. The lack of requirement for lattice mismatch allows for this method to not rely on strain, which makes it usable in both lattice matched and lattice mismatched systems.

RHEED patterns during the growth of the [1] droplet QDs was observed along both $[110]$ and $[1\bar{1}0]$ directions as shown in Figure 3-1. After the Ga is deposited the RHEED pattern shows the (2×1) reconstruction and a halo pattern, which is the result of Ga droplets on the surface. When As irradiation starts, the (2×1) surface reconstruction is replaced with a spotty pattern. The spotty pattern is caused by 3D growth on the surface. The decrease of the halo indicates that the Ga droplets turn into GaAs QDs.

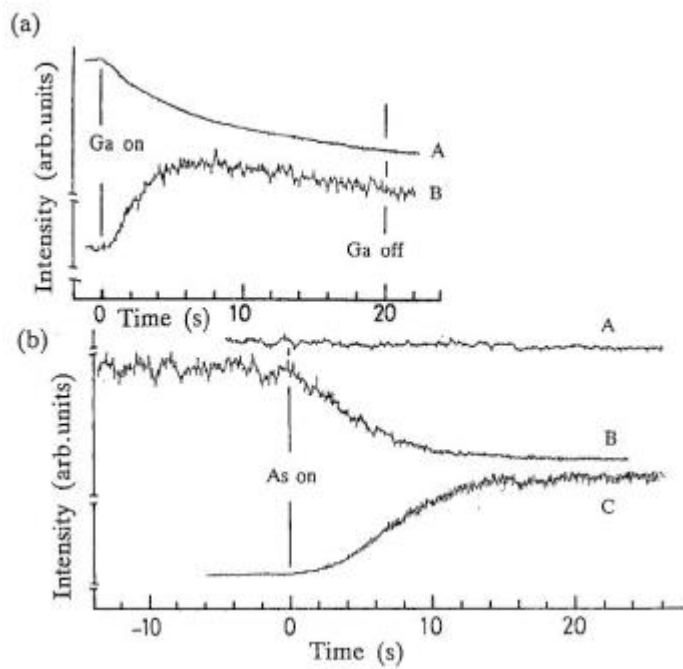


Figure 3-1 RHEED intensity for Ga deposition and As irradiation [1]

The formation of metal droplets are caused by a process called Ostwald ripening. Ostwald ripening is the combination of smaller clusters to form a large cluster. It has been suggested by C. Heyn that Ostwald ripening may occur during droplet growth, the time between Ga deposition and As irradiation, and As irradiation. Figure 3-2 shows that the substrate temperature has a critical effect on Ostwald ripening.

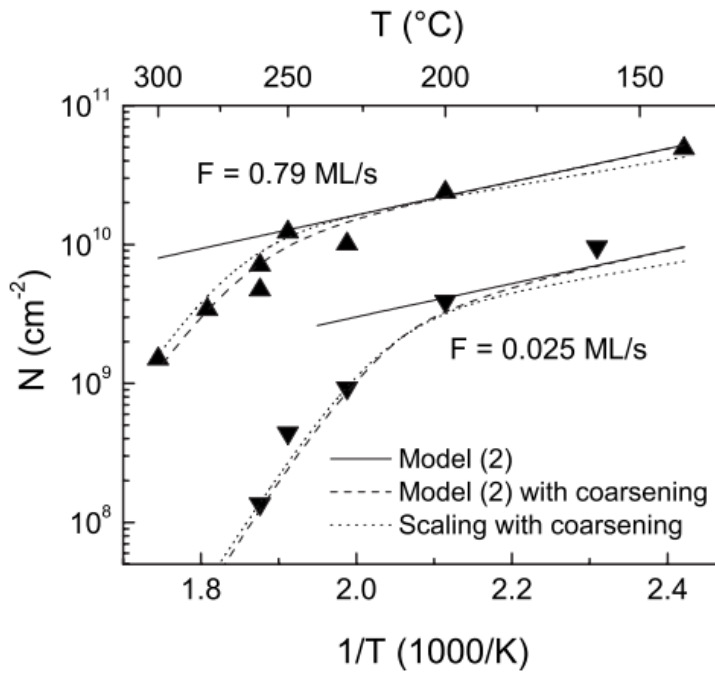


Figure 3-2 Surface density N of GaAs QDs [2]

Control over the size and density of the QDs is a critical factor in realizing certain QD applications. Applications such as quantum cryptography and quantum computing require the use of a single photon source. By definition given by P. Michler et al,[3] a single photon source is “ an optical source emitting a train of pulses that contain one and only one photon”. In order to realize the single photon source with semiconductor quantum dots, isolated measurements of a single QD is required. Thus, by controlling the density of the quantum dots such that the space between quantum dots are substantially large, single quantum dots may be isolated for use of single photon sources.

In order to control the density of the QDs, the density of droplets must be controlled. As seen in Figure 3-2, the density of the droplets is directly affected by the temperature of QD growth. Figure 3-3 shows AFM images of droplets at various growth temperatures and the change in density.

Droplets are typically formed at temperatures lower than typical self-assembled QD growth. For this reason, droplet growth temperatures were scanned at temperatures of 300°C and above. The droplets were deposited on an $\text{Al}_{0.3}\text{Ga}_{0.7}\text{As}/\text{GaAs}$ substrate under growth speed of 0.5 ML/s [4] The 50nm AlGaAs layer is grown on the (100) GaAs substrate at 600°C. A total 2 monolayers of Ga were deposited on the AlGaAs surface. The density of the droplets decreases rapidly above a certain temperature of 350°C. This is due high migration of the surface metals at increased temperatures. However, the diameter and height of each droplet increases as the Ostwald ripening is increasingly active at higher temperatures.

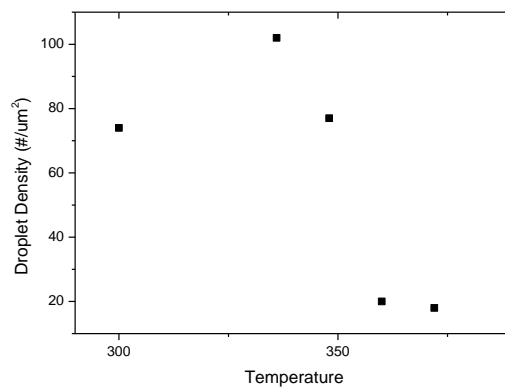
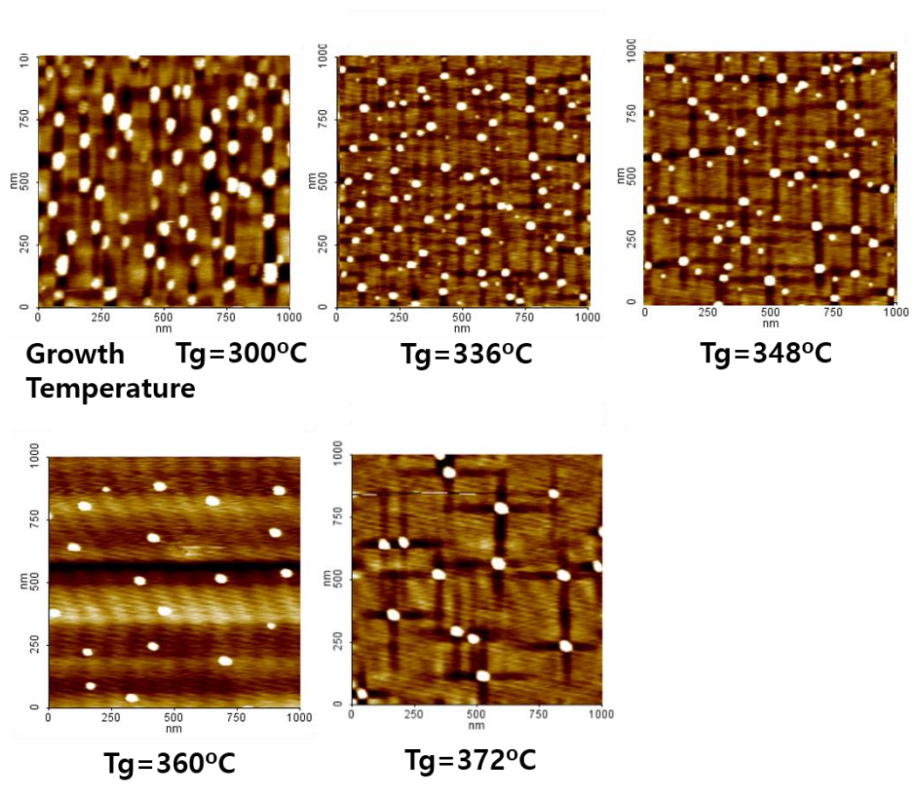


Figure 3-3 Temperature dependence of droplet density

Another factor which is studied closely is the beam equivalent pressure or flux of the applied metal. Once the substrate temperature has been chosen for the appropriate range of droplet density other factors are studied for the fine tuning of size of the droplets. Two of these factors is how much metal would be deposited and how much time would be allowed for the metal to migrate. The effect of total amount of metal deposited is trivial. Greater amounts of Ga results in high density of droplets or increased size of droplets depending on the growth temperature. To find the effects of Ga migration over the surface the total amount of Ga was fixed and the flux rate of the Ga was varied. Figure 3-4 shows AFM images of Ga droplets deposited at a deposition temperature of 360°C where a total of 2 monolayers of gallium is deposited on the substrate. The flux of the Ga is varied from 1/32 ML/s to 1/2 ML/s. This also means that the deposition time of the Ga ranges from 2 seconds to 64 seconds. As the flux is increased (i.e. time is decreased) the diameter of the droplet increases due to greater surface migration of the Ga metal. The density also increases with greater flux as expected.

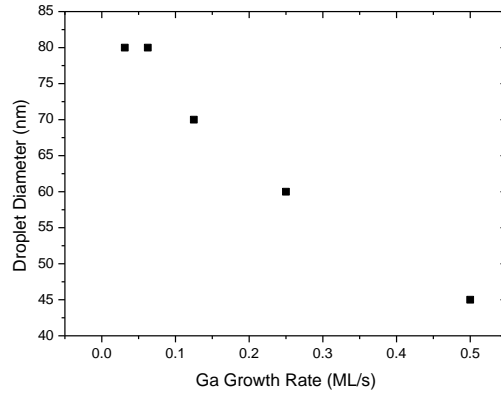
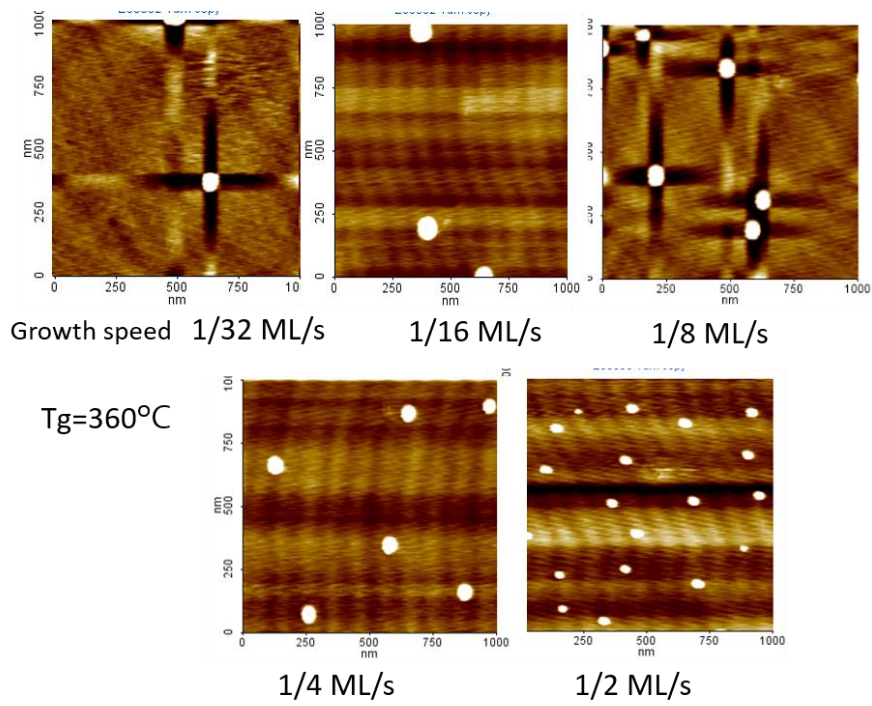


Figure 3-4 Flux dependence of droplet diameter

The second step in the formation of DE QDs, is the arsenization process. K Reyes modeled this process as a competition between the wicking and crystallization processes.

[5] The velocity v_n of the GaAs front under an As deposition rate F_{As} is given as

$$v_n = glF_{As}$$

where l is the spacing of the lattice and g is the factor that depends on the shape of the liquid region and difference in the As adsorption probability. Simultaneously to the growth of the GaAs front, Ga atoms are moved away from droplet by As. The time scale of this process is given by

$$\tau = \frac{1}{F_{As}}$$

and the diffusion length scale is

$$\lambda = \sqrt{\frac{D'_{Ga}}{F_{As}}}$$

where D'_{Ga} is the diffusion coefficient. This results in a wicking velocity

$$v_w = l^2 R_0 \exp\left[-\frac{E'_{Ga}}{k_B T}\right]$$

When $v_w \ll v_n$ fully crystallized quantum dot forms due the crystallization process being dominant. However, if the wicking process is comparable to the GaAs growth ie. $v_w \sim v_n$, the fronts may fail to coalesce, resulting in a nanoring. This is illustrated in

Figure 3-5.

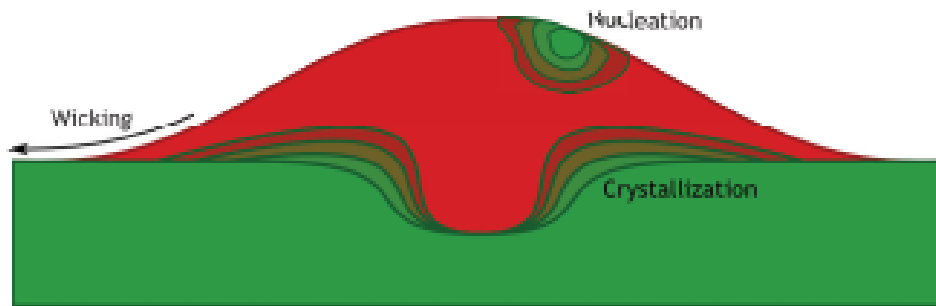


Figure 3-5 Schematic of kinetic processes that determine nanostructural development [5]

The AFM images of the arsenization process is shown in figure 3-6. The AFM images show the different structures depending on the arsenic deposition rate. When a sufficient amount of As is applied the droplets transform into a whole quantum dot. As the amount of arsenic is decreased, it is apparent that the speed of the wicking process becomes more dominant. A small decrease in As causes the droplet to split into two parts, resulting in a coupled QD formation. Even less As causes the droplet to reveal a hole in the center of the structure. The nanostructures with holes become more flat as less arsenic promotes the wicking compared to the crystallization. The extreme case where no As is applied will be discussed in following sections.

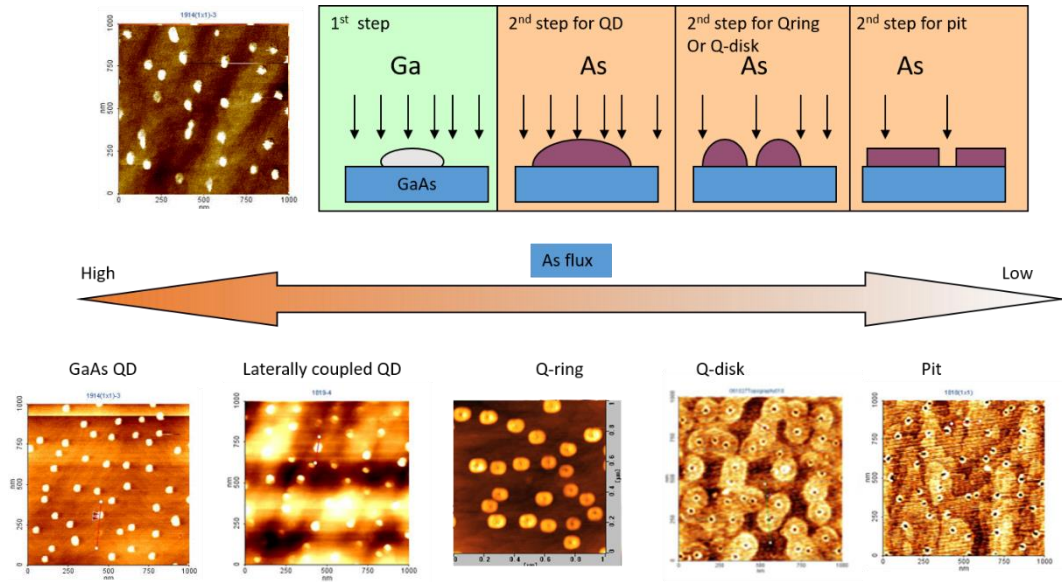


Figure 3-6 AFM images of different nanostructures in the droplet arsenization process[4]

3-2 Internal thermal heating

The optical quality of a quantum dot is crucial for quantum optic applications. Therefore semiconductor QDs are normally grown by a S-K mode with a capping layer which exceeds 50nm to preserve the optical quality of the QD.[6] However, in order to couple the QDs to near-field confined modes, the QD must be close to the metal-dielectric interface where the plasmonic modes exist[7]. Attempts to observe plasmonics have been unsuccessful with droplet QDs due to a thick capping layer and subpar optical quality.[8]

Previous researches for QDs with thin capping layers have used GaAs filled nanoholes. [9,10] However these QDs have a capping layer with a minimum thickness of 10nm and broad linewidth in optical properties.[10]

The size, shape and density are critical factors to control the optical characteristics of QDs. As seen in the previous section, it is possible to grow low density QDs with droplet epitaxy. However, since droplet epitaxy relies on the separation of group III and group V materials, a post annealing process is required to improve the crystal quality of the QDs.[11] However high temperature annealing is known to deform the QD[12], thus a thin capping layer is deposited to avoid the deformation of QDs. [13] For this reason, an internal thermal heating (ITH) method was introduced. ITH allows for better control of size and shape of the QDs while annealing in an ultra high vacuum chamber.

Figure 3-7a shows the growth process for the QDs grown with ITH. The first part of the growth follows the growth of droplet quantum dots. Preparation of the substrate is done

by growing an AlGaAs layer on a GaAs substrate. The Ga Droplets are deposited at a substrate temperature of 321°C. The total Ga deposited was 2ML with a flux equivalent to 0.5ML/s. To achieve uniform growth, an interruption time of 10s is given after the deposition of Ga droplets. An As flux of 1×10^{-5} torr is injected on the Ga droplets at room temperature. After the arsenization process, the substrate is raised to the ITH temperature. The As flux at ITH is 6×10^{-6} . This ITH process is maintained for 10 minutes. As previously reported[14], the ITH process causes the emission of the QDs to blueshift, due to a change in the size and shape of the QDs. At this point, growth is stopped for samples required for AFM measurement. To finalize the growth of ITH grown QDs, an AlGaAs capping layer is deposited on the GaAs QDs. This process is done in two steps, first an 8nm thick layer is deposited at 563°C then a 3nm layer is deposited at a higher temperature of 580°C. The capping layer at a high temperature is expected to increase the optical quality of the QDs.

AFM measurements reveal that height of the QDs can be controlled by the ITH process with no significant change in QD width and density. (Figure 3-7 b-d) As the ITH temperature increases to 500°C, the height of the GaAs QDs decreases slightly. For ITH temperatures above 500°C, material loss causes the height of the QDs to decrease rapidly. This is apparent from the lack of change in the density of the QDs. It is therefore concluded that above ITH temperatures of 500°C, the reduction of material causes the QDs to change in size and shape without any surface movement.

The height of the QD, at the temperature of 563°C, is measured to be 8.7 ± 3.4 nm. The QDs are then capped with an AlGaAs layer of 11 nm. As seen in Figure 3-7 b., The width

of QDs and droplets remain unchanged during the arsenization process and ITH process. The height of the GaAs QDs is about twice of the droplets during arsenization and decreases at higher ITH temperatures. Such trends are clearly apparent in Figure 3-7 c. where the aspect ratio of the QD and droplets are given. The elongation of the QD shape is attributed to the different diffusivity (along [1 1 0] and [1 -1 0]) of Ga on GaAs [0 0 1].[15]

The density of Ga droplets and GaAs QDs with and with ITH process shown in Figure 3-7 d. suggests that the Ostwald ripening effect is minimal once the arsenization process has been finished. Contrary to droplets, which we have shown in the previous section to vary in density when the substrate temperature is changed, arsenized droplet QDs show a constant density for different substrate temperatures during ITH. In order to minimize the deformation of the QDs during the ITH process, an As atmosphere of 6×10^{-6} Torr is maintained. The control of height without any change in width and density of the QDs allows us to use this method for even thinner capping layers while maintaining the optical quality and quantum confinement effects.

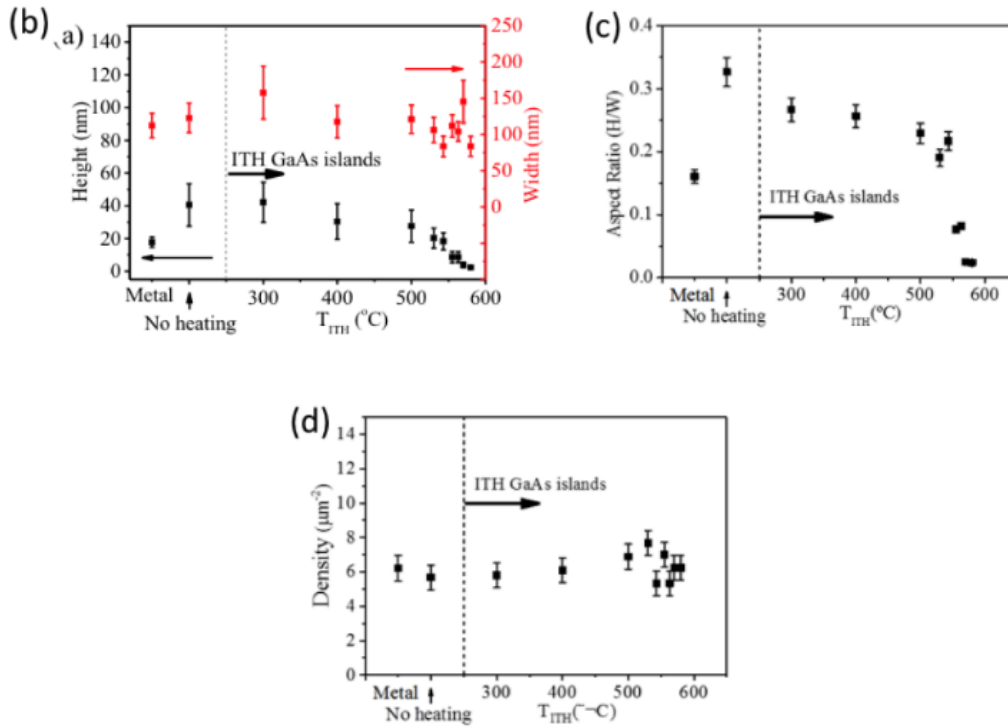
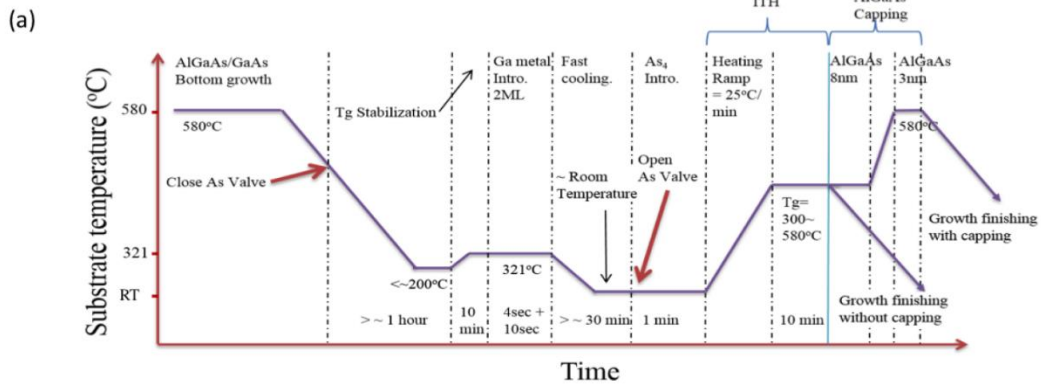


Figure 3-7 a) GaAs droplet QDs growth procedure with an internal thermal heating step b) Dimensions (width and height), c) aspect ratio (height/width) and d) density of the QDs with no ITH and as a function of ITH temperature

Figure 3-8 b. shows a SEM image of the AlGaAs capped GaAs QDs. Due to the thin capping layer the quantum dots below the capping layers are visible with the SEM. The shape of the QDs are elongated along the [1 -1 0] direction, with height and width of the surface features of 3.8 ± 1.0 nm and 208.3 ± 42.5 nm. AFM scanning of the surface in figure 3-8 c. and d. agree with this result.

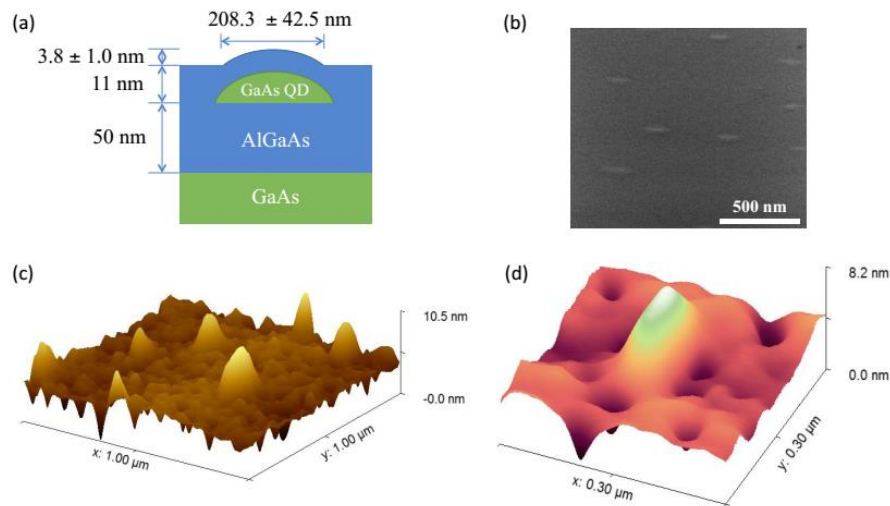


Figure 3-8 (a) Schematic of the droplet QDs (b) SEM of droplet QDs (c) wide range AFM showing the density of the QDs. (d) AFM image of a single QD

The optical properties of the QDs were characterized by photoluminescence imaging and micro-photoluminescence spectroscopy. The sample was illuminated with a 455nm LED, at cryogenic temperatures. Figure 3-9 a. shows several emitters, proving that

most of the QDs are optically active. We then select a single emitter, with an excitation spot size of $2\mu\text{m}$ in diameter. Figure 3-9 b. shows sharp emission lines with a linewidth as low as 0.175 nm at a wavelength of 730 nm . The PL results prove that the QDs with an ultra thin capping layer allow a quantum confinement effect of the carriers and stable emission in the visible range. The proximity to the surface due to a thin capping layer is known to broaden the emission lines [16] By varying the excitation power, as shown in figure 3-9 c. the brightness of the emitter can be assessed. The emission intensity is plotted as a function of laser pump power. The reproducibility of the excitation at high powers proves the stability of the QDs, even with a thin capping layer.

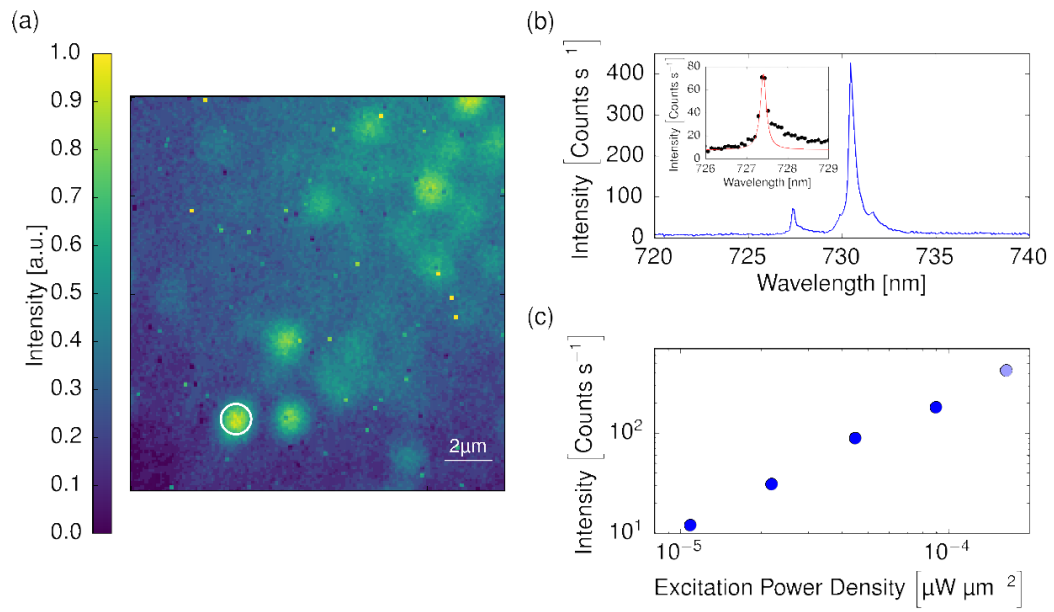


Figure 3-9. a) Photoluminescence image showing the emission of several QDs, collected under 455 nm LED illumination. b) Photoluminescence spectrum collected under 405 nm continuous-wave laser excitation with power density of $1.8 \times 10^{-4} \mu\text{W } \mu\text{m}^{-2}$, at a temperature of 4.7K. c) Emission intensity plotted as a function of laser excitation power for the emission line at 730.5 nm shown in b.

3-3 Droplet drilled holes

The arsenization process which was discussed in the previous section is revisited for an extreme case, where the no external arsenic is applied during the arsenization process. During this extreme case, the only As that engage in the arsenization process is the As atoms diffused from the GaAs substrate through the Ga droplet and the residual As atoms in the chamber. In such a scenario, the arsenization process modeled in the previous section is no longer valid because it models the two processes competing against each other with the As flux. Under an extreme condition such as this requires a modified model. C. Heyn suggested such a model where the droplet would etch the substrate underneath. This is shown in Figure 3-10.

The kinetic model which C. Heyn reported assumes that during the annealing process of a Ga droplet on a GaAs substrate, desorption removes the droplet material from the droplet surface. The rate at which this happens is given by :

$$R_D = \nu \exp\left[\frac{-E_D}{k_B T}\right]$$

where the activation energy is given by E_D .

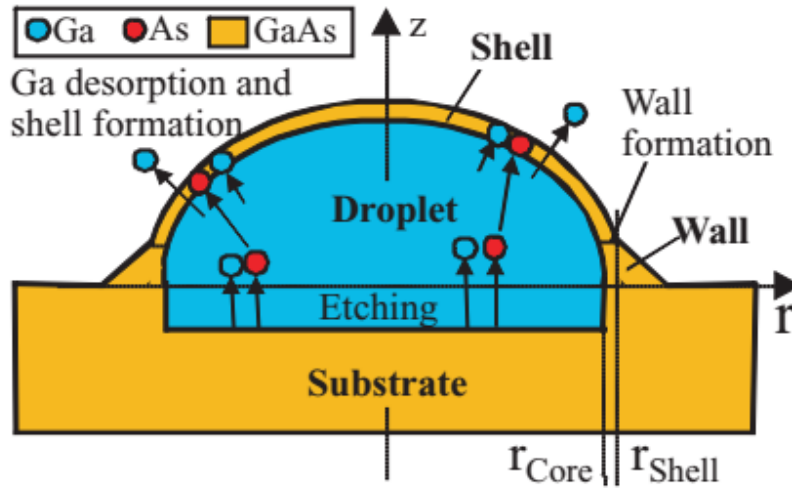


Figure 3-10 Scheme of the droplet geometry and the processes considered in the core-shell model. [17]

The etching of the substrate is caused by the diffusion of As atoms into the liquid droplet by the concentration gradient. The etching rate is given by

$$R_E = (x_{As,max} - x_{As}) \nu \exp\left[\frac{-E_E}{k_B T}\right] \text{ for } x_{As,max} > x_{As}$$

and

$$R_E = 0 \text{ for } x_{As,max} \leq x_{As}$$

Where $x_{As,max}$ is the maximum solubility in liquid Ga and the As concentration is $x_{As} = N_{As,core} / (N_{Ga,core} + N_{As,core})$. The removal of As causes the liquefaction of the

substrate at the interface between the droplet. If the diffused As is not removed the etch process will stop.

A third process where the shell and wall are formed allows the etching process to continue. Desorption of Ga atoms at the surface of the droplet causes a local increase in As concentration and exceeds maximum solubility. GaAs is crystalized at these points and a thin GaAs shell is formed. The rate is given by

$$R_S = x_{As} \nu \exp\left[\frac{-E_S}{k_B T}\right]$$

During the last process the GaAs shell is deposited at the edge of the droplet, which rate is given by

$$R_C = \nu \exp\left[\frac{-E_C}{k_B T}\right]$$

The time evolution of Ga and As atoms at the droplet core and shell are given by the following equations.

$$\frac{d}{dt} N_{Ga,core} = - \left(\frac{S_{core}}{V_{Ga}^{\frac{2}{3}}} \right) R_D + \left(\frac{A_{core}}{V_{GaAs}^{\frac{2}{3}}} \right) R_E - \left(\frac{S_{core}}{V_{Ga}^{\frac{2}{3}}} \right) R_S$$

$$\frac{d}{dt} N_{As,core} = \left(\frac{A_{core}}{V_{GaAs}^{\frac{2}{3}}} \right) R_E - \left(\frac{S_{core}}{V_{Ga}^{\frac{2}{3}}} \right) R_S$$

$$\frac{d}{dt} N_{Shell,(Ga,As)} = \left(\frac{S_{core}}{2} \right) R_S - \left(\frac{A_{Shell}}{2} \right) R_C$$

where S is the surface area, A is the interface area, and V is the volume.

The hole depth is given by

$$\frac{d}{dt} z = -V_{GaAs}^{1/3} R_E$$

and the wall height is given by

$$\frac{d}{dt} z = V_{GaAs}^{2/3} R_C$$

The calculation of the discussed model is graphed in figure 3-11.

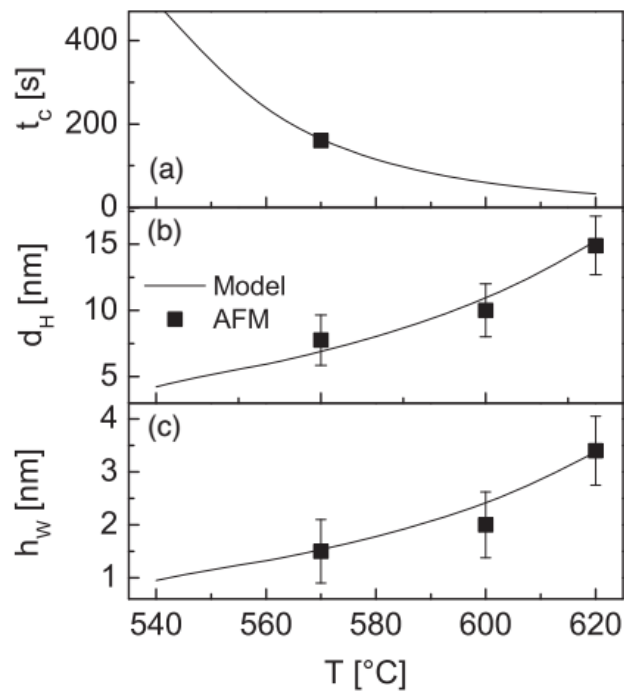


Figure 3-11 Calculated and measured temperature dependence of (a) the critical time t_c up to hole formation, (b) the hole depth d_H , and (c) the wall height h_w . [17]

According to the model, the depth of the etched holes reach up to 15nm in depth at temperatures of 620°C. The walls surrounding the etched hole increases as the holes get deeper, depositing the removed As around the hole. The critical time in which the Ga metal in the droplet is used up, decreases to a few seconds at higher annealing temperatures, meaning that the Ga desorption is rapid.

This droplet etching also named droplet drilling in this thesis, has very unique properties that can be exploited for QD applications. Because droplet drilling uses Ga droplets to etch the substrate, droplet drilling shares many properties used in droplet growth. The density of the holes may be controlled by droplets and the amount of Ga which is critical in the drilling of the hole is controlled by the size of the droplet. Another interesting characteristic of the droplet drilled hole is the shape of the hole is directly affected by the shape of the droplet. Since the metal droplet is not affected by the surface tension of the lattice, a typical Ga droplet is in the shape of a circle. Figure 3-12 shows AFM images of a droplet drilled hole. Measurements along perpendicular axes show that the hole is indeed symmetrical. The circular symmetry of a droplet drilled hole is an important property that can be exploited to improve single photon sources to emit entangled pairs of photons. Further discussion of this topic will be in later sections.

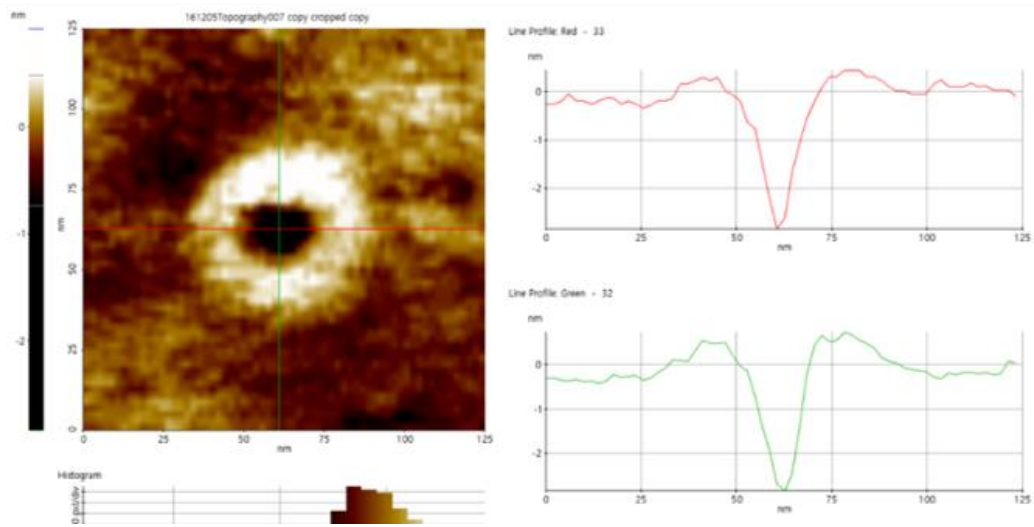
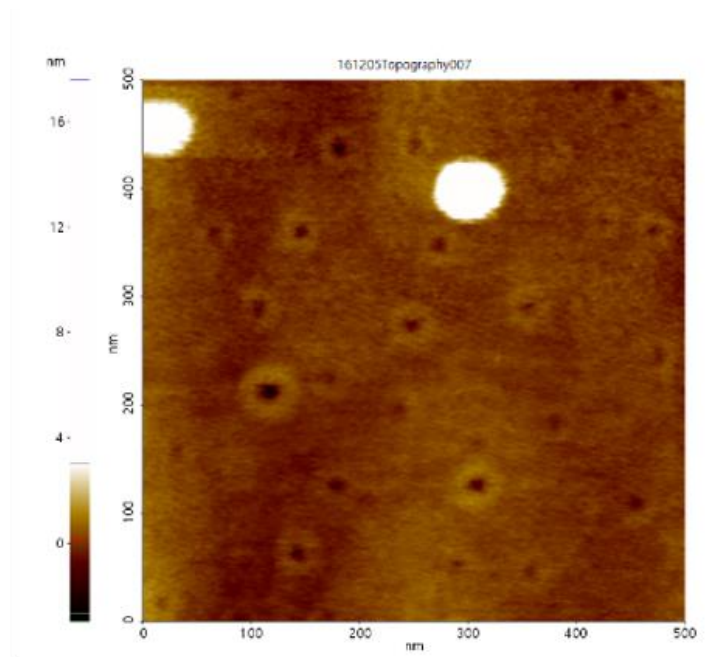


Figure 3-12 AFM image of a droplet drilled hole and the symmetry along perpendicular axes.

TEM images of the cross section of a hole are shown in Figure 3-13. A single layer of phosphorus is deposited to highlight the interface between the droplet drilled substrate and the GaAs capping layer. It is apparent from the cross section image that the Ga droplet has etched the GaAs substrate with a depth of a few nanometers. This agrees with the data collected from the AFM images.

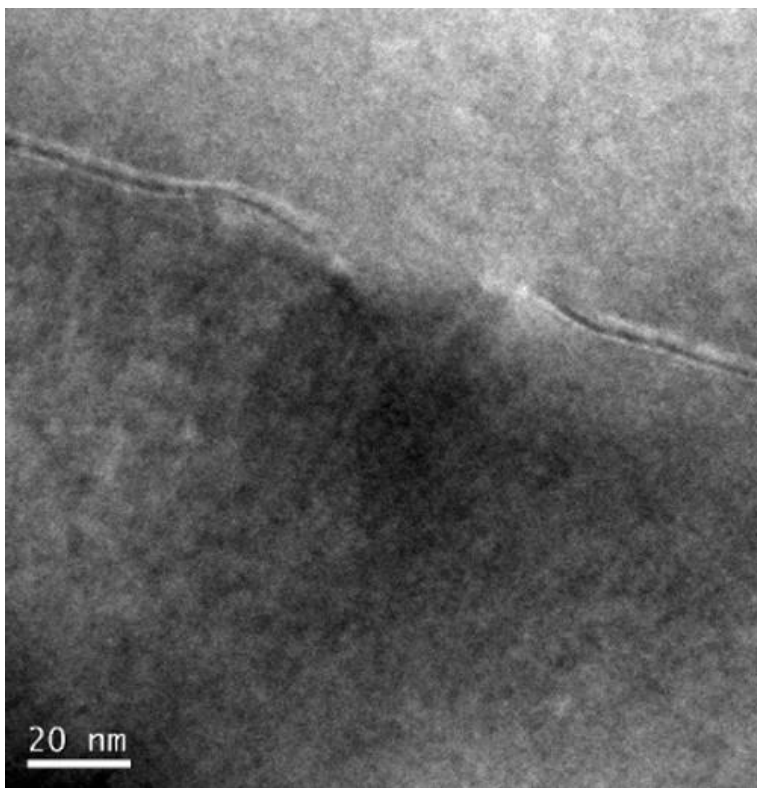


Figure 3-13 TEM image of a droplet drilled hole. The interface is highlighted by a single layer of phosphorus.

The growth process of droplet drilled holes follow the footsteps of droplet epitaxy. After the growth of an GaAs buffer layer, substrate temperature is lowered and the As flux is quenched. Figure 3-14 describes the following steps for a basic droplet drill. Once the residual As has settled, the substrate temperature is raised to a certain temperature around 300°C. After the Ga droplets are deposited under preferred conditions, the substrate temperature is raised to an annealing temperature.

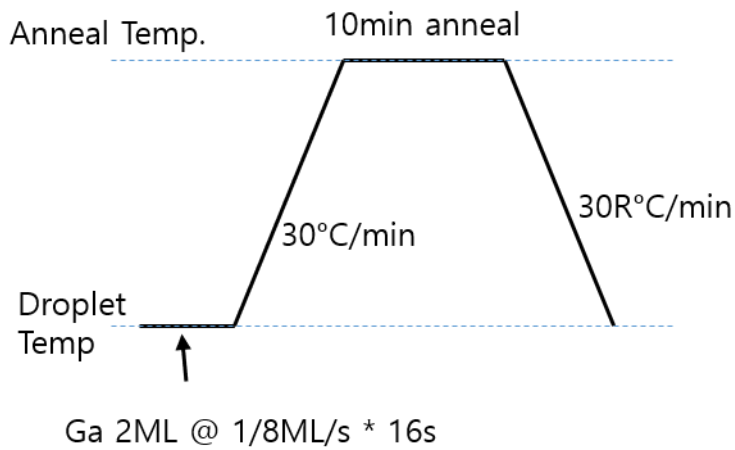


Figure 3-14 Basic growth process of a droplet drilled hole.

AFM images in figure 3-15 show the change in droplets as the annealing process progresses. Figure 3-15 b. shows the Ga droplets starting to remove the As from the substrate with a few droplet already forming holes. After 10 minutes of annealing, many of

the droplets have formed holes. The AFM images show non optimized conditions for droplet drilling. For this reason, few of the droplets form islands rather than holes. This is presumably due to excess amount of Ga metals migrating at high temperatures to form larger Ga droplets.

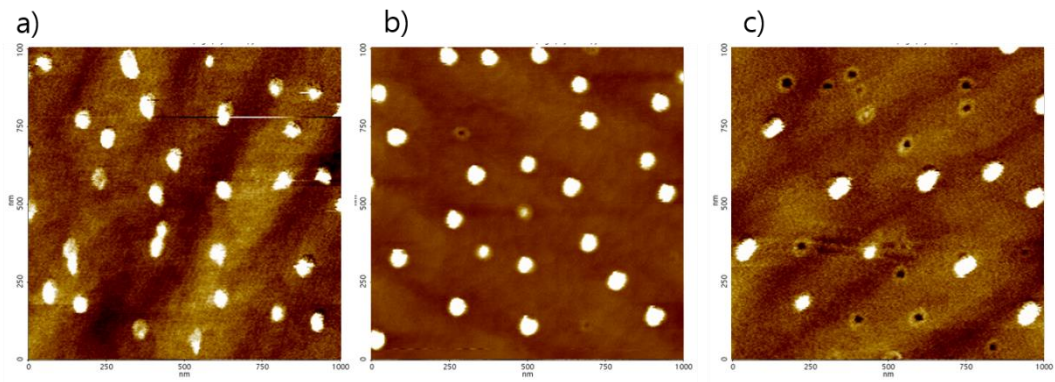


Figure 3-15 AFM images of a) Ga droplets, b) Ga droplets raised to the anneal temperature and cooled, and c) Ga droplets annealed for 10 minutes.

Annealing temperature of the droplets are also a critical factor in studying the parameters of droplet drilling. Figure 3-16 shows the AFM image of droplet holes annealed at various annealing temperatures for 10 minutes. It is clearly apparent that with increased anneal temperatures the drilling of the holes is accelerated up to a critical time as explained in the droplet etch model. Similar to figure 3-15 residual Ga islands are formed randomly. For higher anneal temperatures these islands must have increased in size due to Ostwald

ripening as can be seen by comparing the Ga droplet islands of figures 3-16 c. and d.

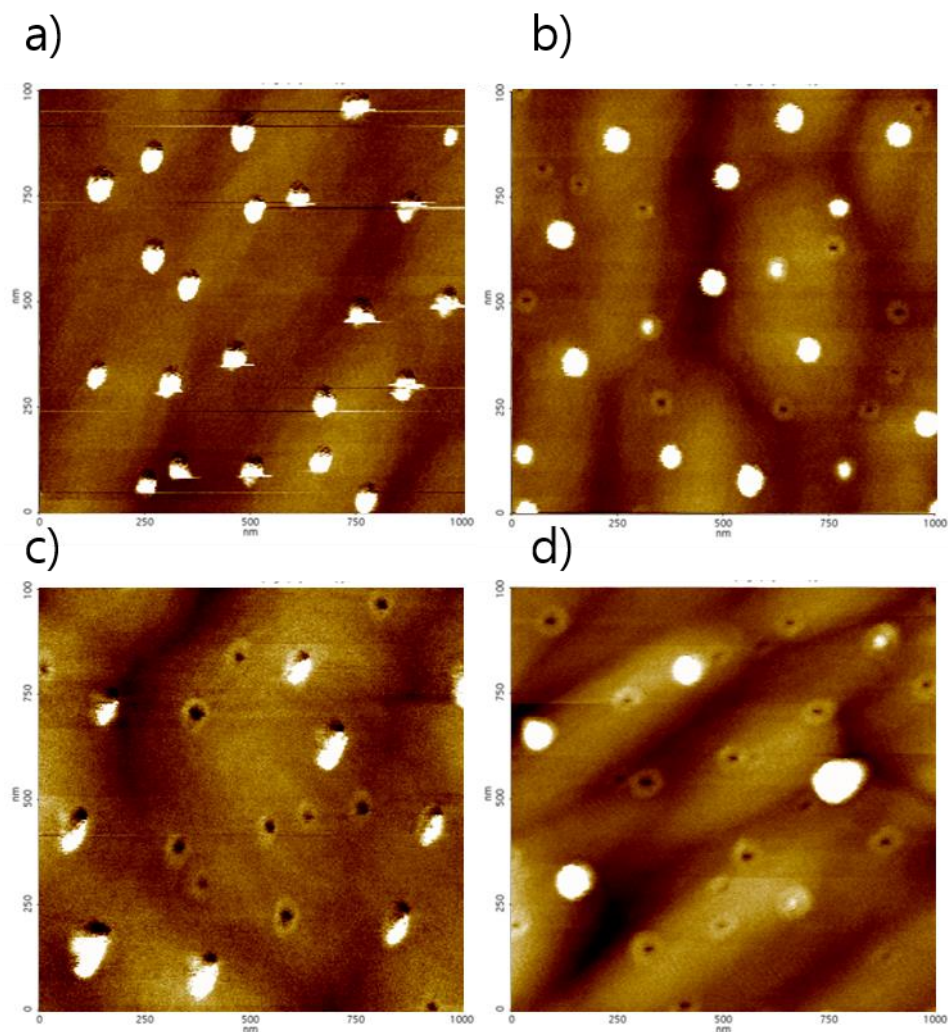


Figure 3-16 AFM images of Ga droplets with a) no annealing, b) 443°C anneal, c) 460°C anneal, and d) 480°C anneal

3-4 Additional Drilling of Holes and InAs Filling

Droplet drilled holes have been used by researchers to realize symmetrical quantum dots. [18] These QDs show great symmetry for emission of highly indistinguishable entangled photons. Most of these researches use Ga or Al droplets on AlGaAs layers to form nanoholes and fill the holes with GaAs to fabricate a GaAs QD. Although these GaAs QDs show excellent optical quality, applying this technique to InAs QDs would open up various new opportunities for quantum optical devices.

According to the droplet etch model in the previous section, temperatures above 540°C are required to etch a hole deep enough for InAs filling (Figure 3-11). However, a high annealing temperature come with a few drawbacks. Without any arsenic to keep the Ga atoms in place the GaAs surface is damaged at high annealing temperatures. This is apparent in figure 3-17, where the GaAs surface had deep pits after annealing of droplets at an annealing temperature of 480°C. For this reason, the annealing temperature must be carefully controlled on GaAs substrates so that the GaAs surface is not exposed to high temperature.

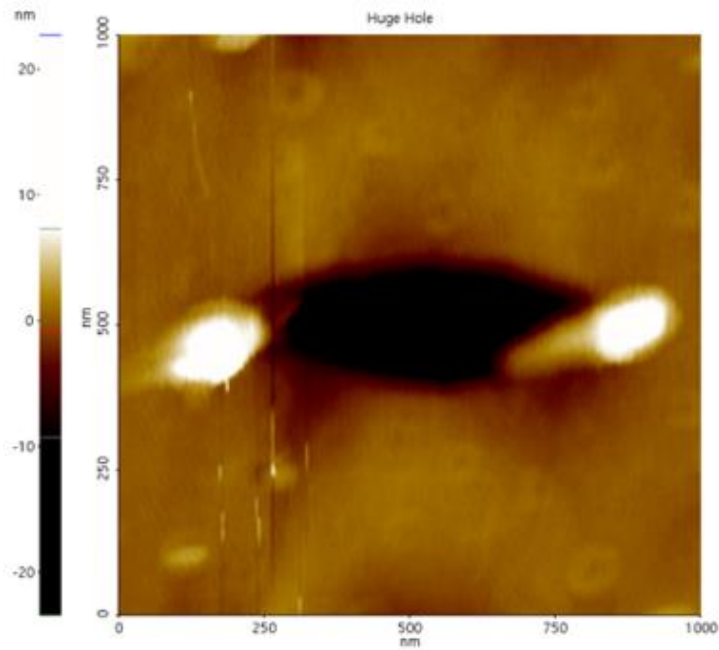


Figure 3-17 AFM image of a pit formed during annealing process of droplet drilling

In order to overcome this obstacle, a multistage drilling technique was designed. Figure 3-18 shows the basic growth sequence of the multistage drilling process. An initial step of droplets is deposited to control the density of the holes. After annealing the droplets to form shallow holes, the substrate temperature is lowered to apply an additional step of Ga droplets. The temperature for additional droplets is higher than the initial droplet stage. This is to allow the Ga metals to migrate over the GaAs surface and find a shallow hole. Once the Ga droplet migrates to a hole it either stays there or move to another site if the diffusion energy of the Ga atom is high enough. Temperature scan of the additional droplet

stage seen in figure 3-19 confirms this assumption. For low temperatures of 336°C, many shallow holes are apparent. This is due to the additional Ga droplets not being able to find its way to the initially drilled holes such that the additional Ga droplets drill their own holes. At high temperatures of 386°C, only a few deep holes are visible. The additional Ga metal was not able to stay in the initial shallow holes and formed Ga islands. Only in a small window of about 30°C around 362°C does the Ga atoms have the appropriate amount of momentum energy.

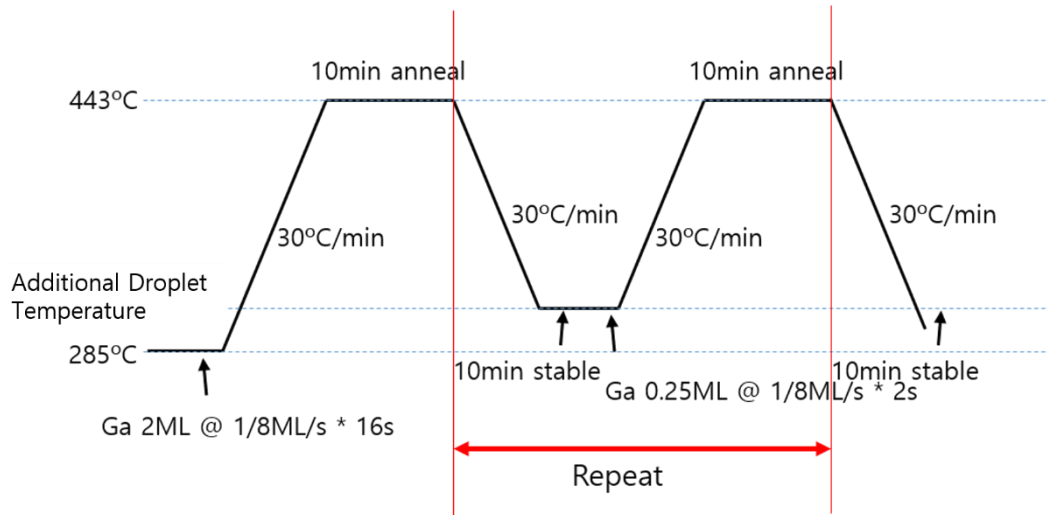


Figure 3-18 Growth sequence of the multistage drilling process.

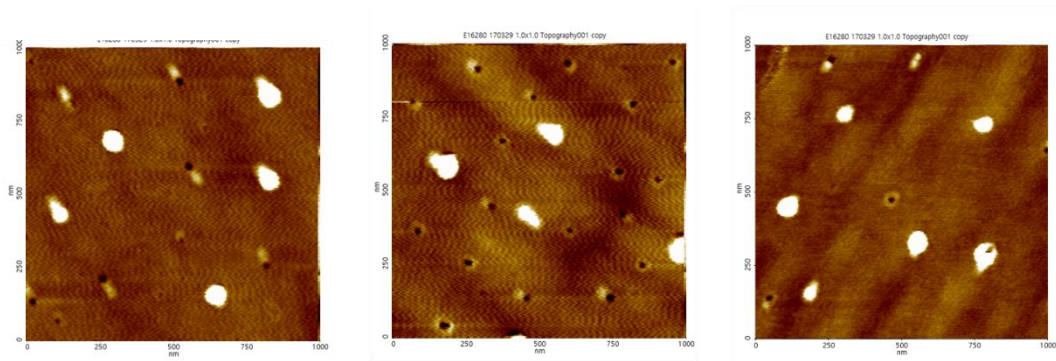


Figure 3-19 Multistage drilling with additional drilling at temperatures of a) 336°C
b)362°C and c)386°C

The additional drilling process is confirmed by applying the additional process multiple times. Figure 3-20 shows the AFM images of GaAs surfaces after initial drilling and after one, three, and six additional drillings. It is apparent that the density of the holes does not change during each additional drilling process. However, the depth of the holes increases for additional drilling processes. This proves that the additional Ga droplets find the initial hole sites and drill each hole deeper without drilling other sites. Figure 3-22 shows a circular shape of the additionally drilled holes which suggests the symmetry.

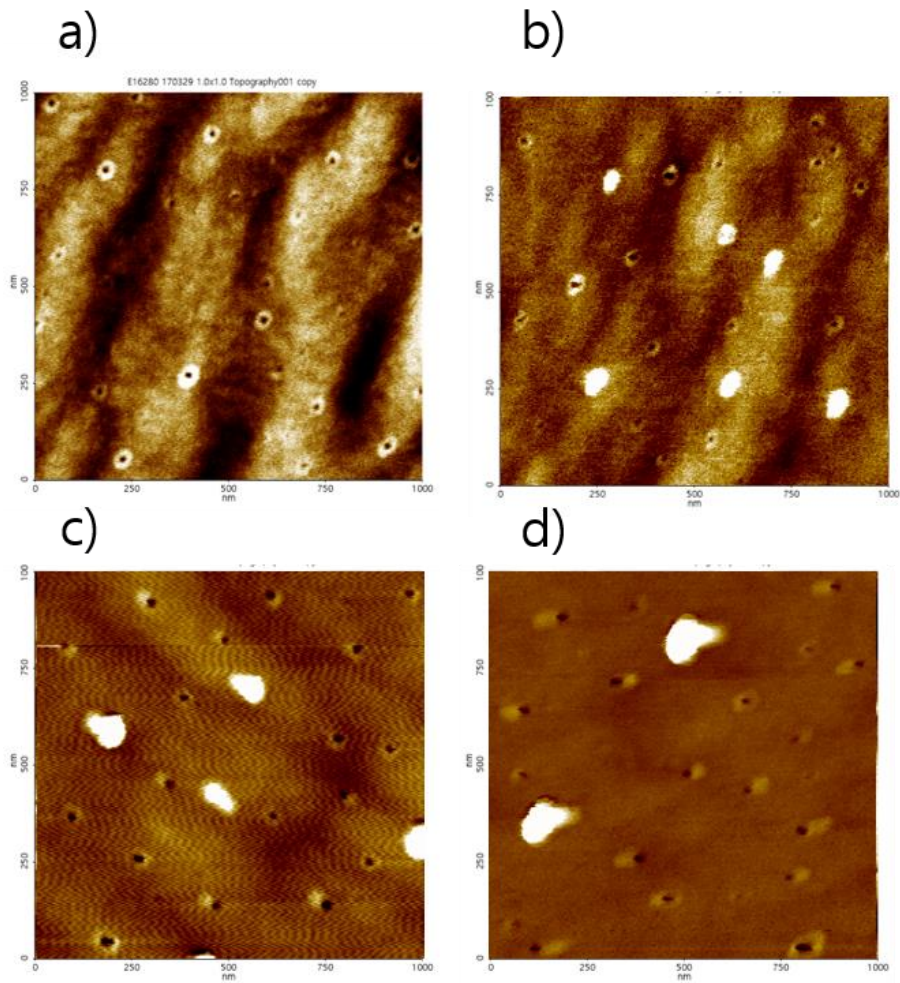


Figure 3-20 AFM image of GaAs surfaces after a) initial drilling and after b)one, c)three, and d)six additional drillings

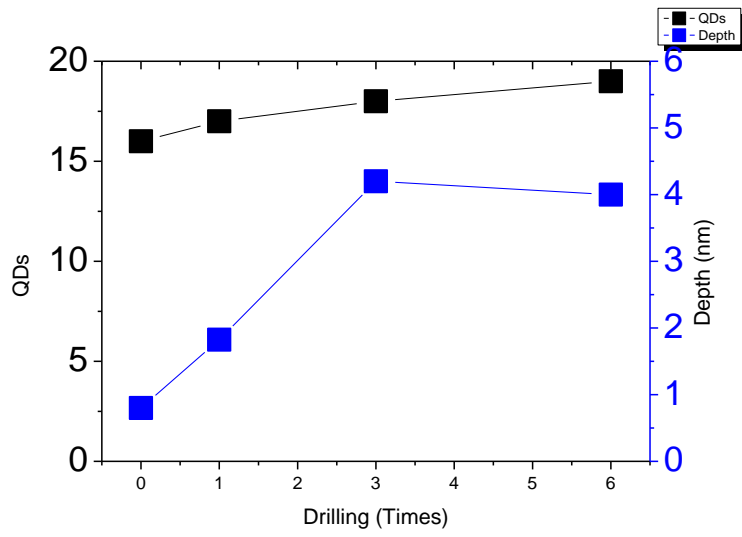


Figure 3-21 Density of holes(QDs) and depth dependence for additional drilling.

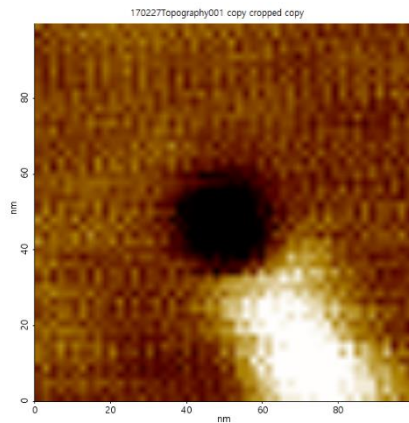


Figure 3-22 Symmetry of multistage drilled hole.

Once the appropriate hole depth is achieved with multistage drilling, the holes are filled with InAs. InAs deposited on a GaAs surface is known to have a S-K growth mode. If InAs QDs are formed on the GaAs surface as S-K QDs, it would be impossible to distinguish the self-assembled QDs from nanohole filled QDs. For this reason, it is preferable for all of the InAs material to move inside the nanohole. Figure 3-23 shows that for InAs deposition of 1.07 ML or less at 480°C, the InAs material moves into the nanoholes whereas increase in InAs deposition form SK QDs.

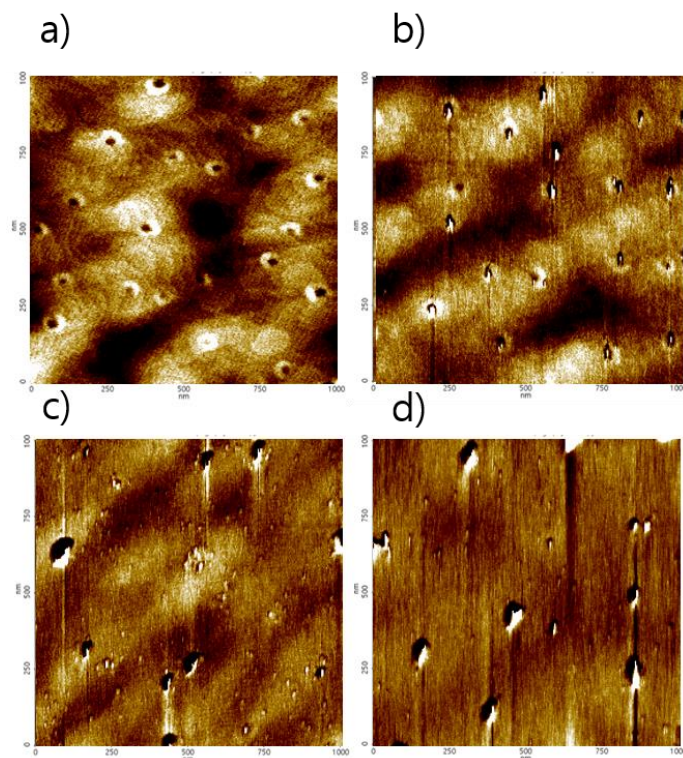


Figure 3-23 AFM image drilled hole surface with an InAs coverage of a) 0.85 ML, b) 1.07 ML, c) 1.31 ML, and d) 1.70 ML

The final stage of the InAs filled nanohole QD growth is the GaAs capping layer that is grown on top of the InAs QDs. The whole sequence of the growth is described in figure 3-24. To promote InAs movement over the surface a low As flux of 2.5×10^{-6} was used during the InAs deposition. AFM visualization of the sequence is given in figure 3-25.

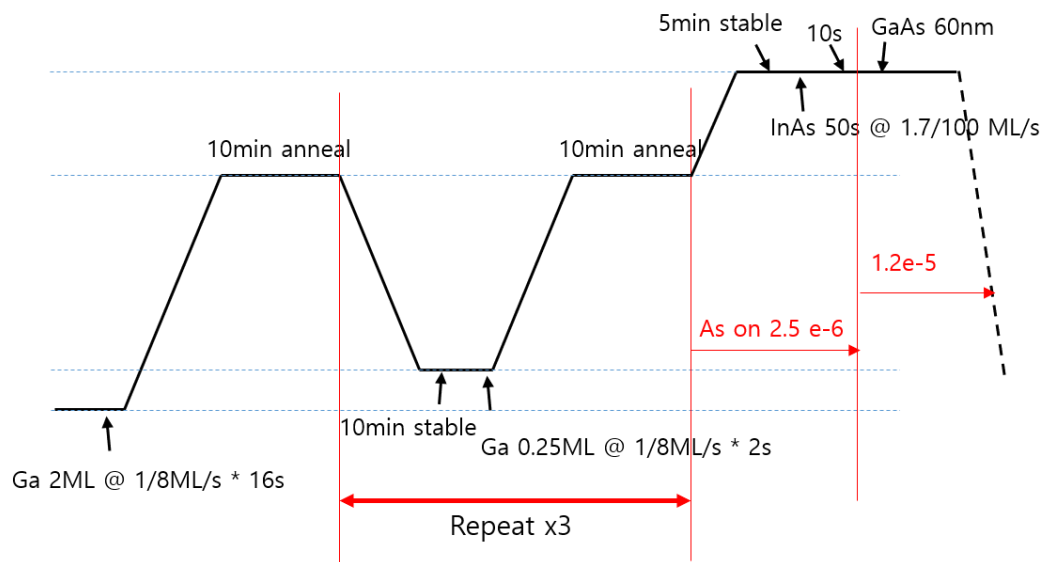


Figure 3-24 Growth sequence of droplet drilled holes filled with InAs QDs.

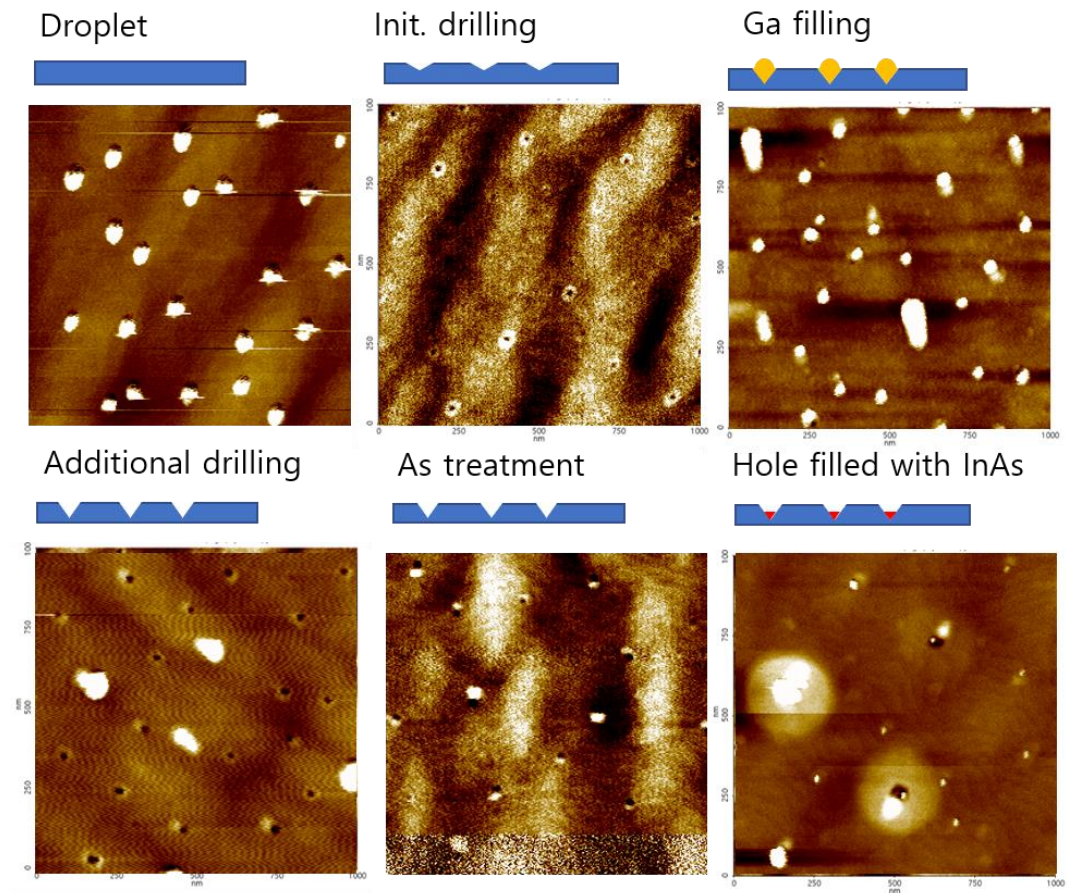


Figure 3-25 AFM image of each step in the growth sequence of InAs filled nanohole QD.

3-5 Summary

Droplet epitaxy and applications of droplet epitaxy were used to grow various types of quantum dots. Control over growth of quantum dots were conducted by i) control of metal droplets, ii) control of arsenization process, iii) control of annealing process and the iv) control of the droplet etching process.

The density and size of the droplets were investigated with various growth conditions. This information acts as a crucial building block for following applications using droplet epitaxy. The density of the droplets can be controlled to be very low such that a single QD can be measured. The arsenization process is a critical part of utilizing droplet epitaxy. Growth of various quantum structures were possible by varying the arsenic flux during the arsenization process. This leads to clues towards other growth methods including droplet drilling.

Droplet epitaxy was used to grow QDs with a very thin capping layer with great optical quality. An internal thermal heating process introduces a method that would increase the optical quality of the QD, while preserving the shape and size of the QD. This allows for the growth of a thin capping layer which can be used for plasmonic applications. The optical quality of the QDs were comparable to QDs with a thick capping layer.

Droplet drilling was investigated in order to use it as a platform for symmetric QDs. The drilled holes follow properties of droplets. This can be exploited to form circular shaped nanoholes. Limitation in control of the anneal temperature is overcome by using a

multistage drilling method. These holes are then filled with indium arsenide to form a symmetric quantum dot. The QDs are then capped with a GaAs layer for quantum confinement. This results in a inverted QD embedded in GaAs matrix.

References

- [1] N. Koguchi and K. Ishige, *Jpn. J. Appl.*, 32, 2052 (1993)
- [2] Ch. Heyn, A. Stemmann, A. Schramm, H. Welsch, W. Hansen, and A. Nemesics, *Phys. Rev. B* 76, 075317 (2007)
- [3] P. Michler, A. Kiraz, C. Becher, W.V. Schoefeld, P.M. Petroff, Lidong Zhang, EHu, A. Imamogulu, *Science* 290,2282 (2000)
- [4] E.H. Lee, *Growth and Characterization of III-V semiconductor nanostructures*, Doctoral Thesis
- [5] K. Reyes, P. Smereka, D. Nothern, J.M. Millunchick, S. Bietti, C. Somaschini, S. Sanguinetti, and C. Frigeri, *Phys. Rev. B* 87, 165406 (2013)
- [6] C F Wang, A Badolato, I Wilson-Rae, P M Petroff and E Hu *Appl. Phys Lett* 85 3423 (2004)
- [7] S A Maier *Plasmonics: Fundamentals and Applications* (Berlin, Springer) (2007)
- [8] G. Nougès, Q. Merotto, G. Bachlier, E.H. Lee, and J.D. Song, *Appl. Phys. Lett.* 102, 231112 (2013)
- [9] Ch Heyn, M. Zocher, L Pudewill, H Runge, A Kuster and W Hansen *J. Appl. Phys* 121,044306 (2017)
- [10] M. Pfeiffer, K. Lindfors, H. Zhang, B. Fenk, F. Phillipp, P. Atkinson, A. Rastelli, O.G.

Schmidt, H. Giessen, and M Lippitz *Nano Lett.* 14 197 (2014)

[11] P. Moonm J.D. Lee, S.K. Ha, E.H. Lee, W.J. Choi, J.D. Song, J.S. Kim and L.S. Dang, *Phys. Status Solidi* 6 445 (2012)

[12] M. Jo, T. Mano and K Sakoda, *Appl. Phys. Expresss* 3 045502 (2010)

[13] M. Jo, T. Mano and K Sakoda, *J. Appl. Phys.* 108 083505 (2010)

[14] S. Bietti, J. Bocquel, S. Adorno, T. AMno, J.G. Keizer, P.M. Koenraad and S. Sanguinetti *Phys. Rev. B* 92 075425 (2015)

[15] C. Somaschini, S. Bietti, S. Sanguinetti, N. Koguchi and A. Fedorov *Nanoscale Res. Lett.* 5 1865 (2010)

[16] N. Ha et al *Phys. Rev. B* 92 075306 (2015)

[17] C. Heyn, *Phys. Rev. B* **83**, 165302 (2011)]

[18] D. Huber, M. Reindl, Y. Huo, H. Huang, J.S. Wildmann, O.G. Schmidt, A. Rastelli, and R. Trotta *Nat. Comm.* **8**, 15506 (2017)

4. Optical characterization of quantum dots

4-1 Photoluminescence of a quantum dot

Three-dimensional confinement of carriers results in localized states for electrons and holes in QDs. The discrete interband transition energies between the electron and hole states are called shells. In self-assembled QDs a wetting layer offers a quasicontinuum of delocalized states surrounding the discrete states of the QD. Figure 4-1 shows the energy levels in a self-assembled QD. The number of confined shells is limited due to the finite height of the confinement. Due to the shape of semiconductor QDs, a strong confinement exists in the growth direction and weaker confinement in the WL plane. Only the lowest state is important for the motion in the growth direction due to the strong confinement. Several bound states need to be considered in the in-plane direction. Additionally, the in-plane rotational symmetry results in an angular-momentum degeneracy in addition to the spin degeneracy of the weakly confined states. Here, we consider a QD which has two shells for conduction- and valence-band carriers due to confinement. One s-shell and two p-shell states are available for each spin subsystem. The unexcited state corresponds to filled valence-band states and empty conduction-band states

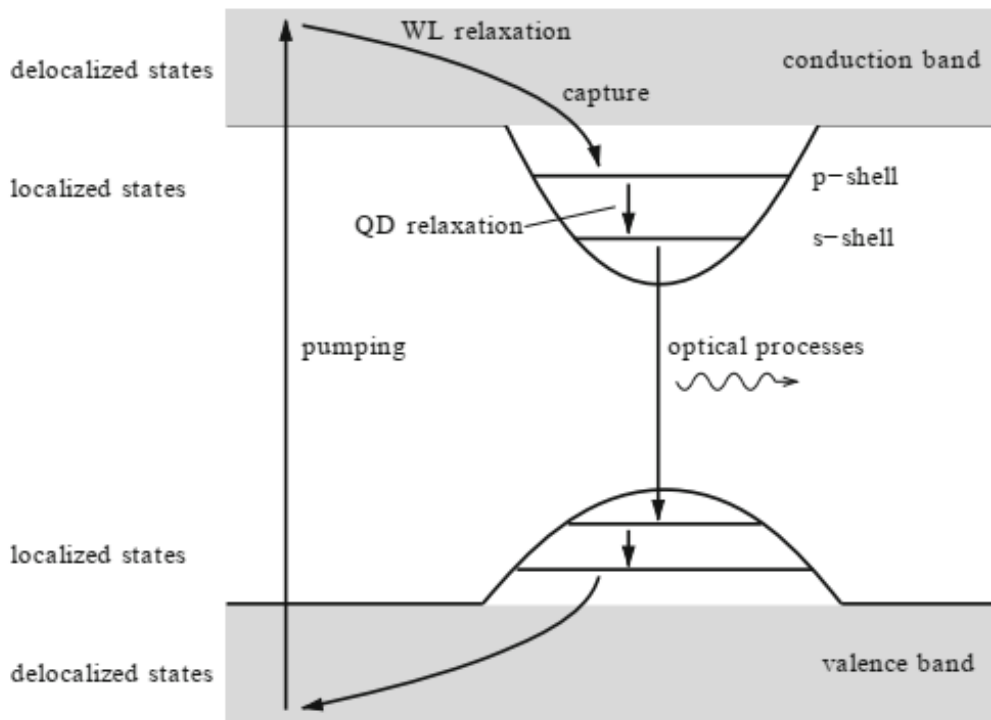


Figure 4-1 Schematic representation of energy levels in a quantum dot (QD) with two shells for carriers in the conduction and valence band, respectively. [1]

An off resonant optical pulse can excite the QD system in order to investigate the optical properties of the QDs. Carriers are formed from the excitation in the barrier-, wetting layer-, or higher QD-states. Figure 4-1 shows the fast relaxation into the lower QD states, which is caused by carrier-carrier and carrier-phonon interaction. [2,3] If the temperature is substantially low and the carrier densities are moderate, only the QD states

are populated by the carriers. Carrier-scattering process is active in the wetting layer without and recombination.

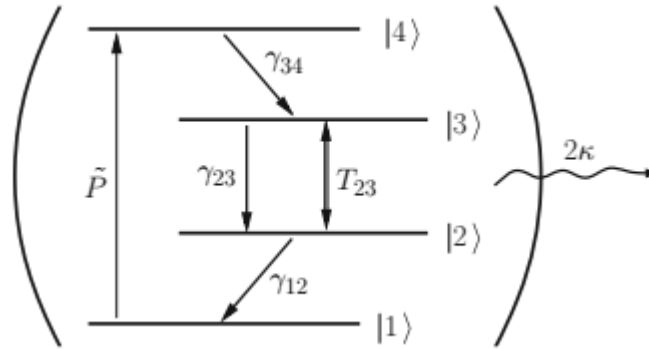


Figure 4-2 Diagram of the atomic four-level laser system. With the pump rate P an electron is excited from the ground state $|1\rangle$ into the pump level $|4\rangle$. [1]

In such a QD system, an atomic four-level system shown in figure 4-2 is used. The main difference of a semiconductor QD is that the unexcited QD system contains filled valence-band states. Conduction-band states may have more than a single electron. It is assumed that only two confined QD shells for electrons and holes (s and p) are considered and the optical pump process is resonant with the p-shells.

Figure 4-3 is modeled with the assumption discussed above. The carriers are optically pumped in the p-states and relaxed to the s-states. Since the valence-band states

are filled for an unexcited system more configurations than figure 4-2 are possible. Figure 4-4 shows the possible configuration for s-states. Recombination is only possible when an electron and a hole are paired.

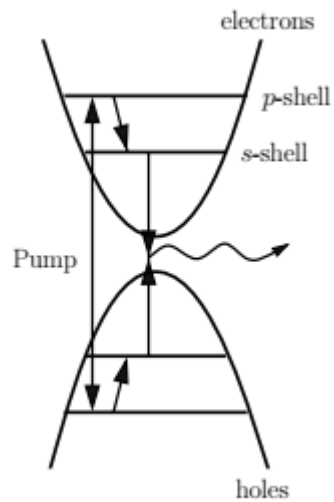


Figure 4-3 QD model with carrier excitation in the p shells and recombination in the s shells

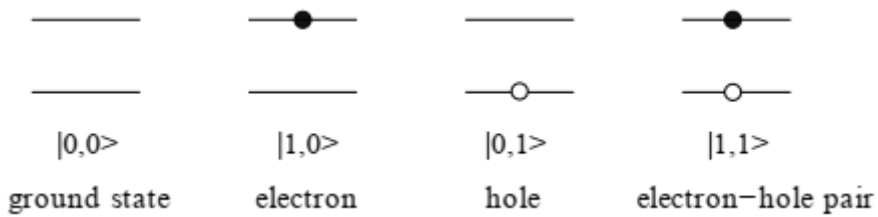


Figure 4-4 Schematic level diagram of possible electron and hole occupations for the s-shell of a quantum dot

For an even number of electron and holes in a QD, recombination from the exciton, the biexciton and multiexcitonic states is observed. Charged exciton transitions take place when an odd number of particles exist in the QD. Coulomb correlations between the carriers causes all transitions to possess distinct and somewhat different energies. By filtering the photons spectrally, all the transitions may be used in principle as a source for single photon emission provided some restrictions are fulfilled. However, biexcitonic or the excitonic transitions are most commonly used. A distinct fine-structure in the emission spectra is observed from these transitions which can be understood through consideration of the spin structure of electrons and holes.

The electronic spin projection along the z-axis of the QD is either $1/2$ or $-1/2$, and the heavy-hole spin projection is either $3/2$ or $-3/2$. Thus for one exciton four distinct spin values are possible in the quantum dot. The two states which have a total z-spin of ± 1 ($| -1/2, 3/2 \rangle$ and $| 1/2, -3/2 \rangle$) are coupled to the light field, while optically decoupled states ($| 1/2, 3/2 \rangle$ and $| -1/2, -3/2 \rangle$) have a total z-spin of ± 2 and are dark due to the selection rules for dipole transitions. When the QD has a perfect cylindrical symmetry around its growth axis, the $\pm |1\rangle$ states are degenerate. However most self-assembled QDs are asymmetric. This causes the degeneracy to be lifted by the electron-hole exchange interaction resulting in a doublet structure. This fine structure splitting is shown in figure 4-5. The fine structure splitting for InGaAs/GaAs quantum dots are in the range of $\sim 0-100\mu\text{eV}$. The excitonic recombination line is split in energy and the individual components are polarized orthogonally.[4] These polarizations are typically aligned with the substrate

cleave directions.

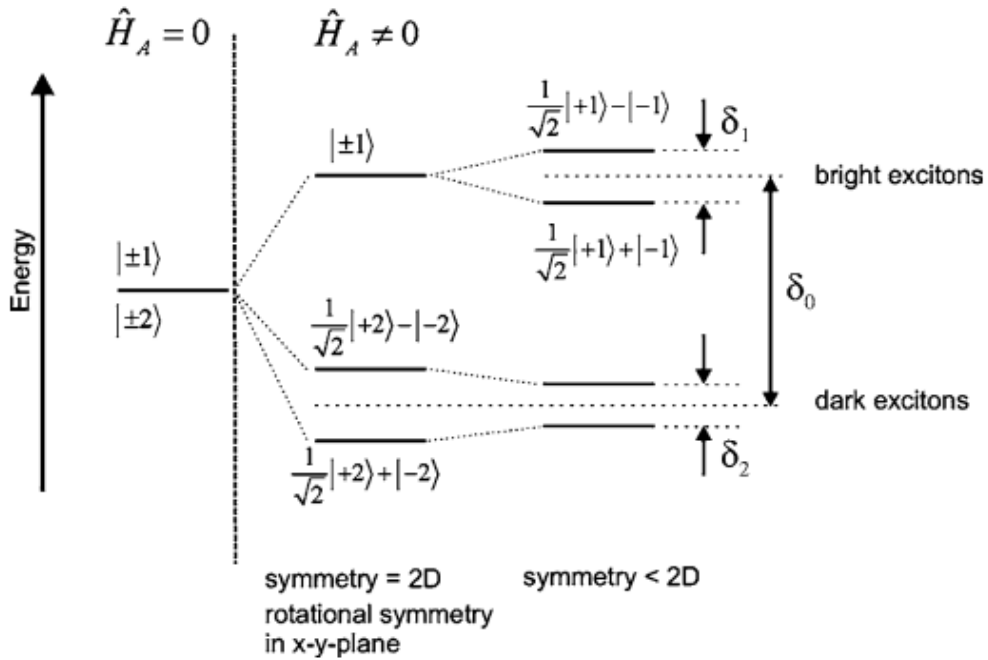


Figure 4-5 Energy level scheme for the excitonic QD ground state without ($\hat{H}_A = 0$) and with ($\hat{H}_A \neq 0$) inclusion of exchange interaction between electron and hole spins.[4]

The biexciton decays into one of the two optically bright excitonic states. It is a spin-singlet state which does not reveal a fine structure itself. For this reason the excitonic states determine the polarization of the biexcitonic recombination. The polarization properties will be discussed in a later section.

A perfect single photon source requires important properties such as an internal quantum efficiency of unity, a predetermined photon emission time (no jitter), and the indistinguishability of the emitted photons. These properties depend on the excitation process. The excitation process is illustrated in figure 4-6.

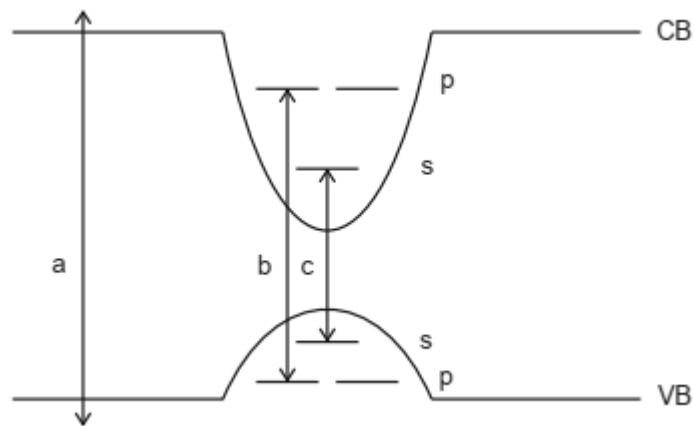


Figure 4-6 Schematic of a) Non-resonant, b) quasi-resonant, and c) resonant optical excitation

For non-resonant excitation, the carriers are excited above the barrier bandgap. Carriers are mainly generated in the barrier and subsequently captured by the QDs and relax to the lowest energy levels within a short time scale ($\sim 1-100$ ps). The resulting multiexcitonic state recombination occurs in a cascade process. Typical radiative lifetimes

of the excitons are in the range of a few 100 ps up to ~ 1 ns. Each excitonic state emits one photon per excitation pulse when the recombination time of the multiexcitonic states are longer than that of the barrier. The non-resonant excitation has drawbacks such as time jitter and line broadening.

Quasi-resonant excitation excites carriers into higher shells. Once the exciton is relaxed into the shell, each generated electron-hole pair recombine to release a single photon. As a result, high quantum efficiency is achievable. Resonant excitation, while ideal, is difficult to implement.

4-2 Photoluminescence of hole filled quantum dot

Quantum dots grown in section 3-4 was measured for photoluminescence. InAs quantum dots with various InAs coverage were excited with an 800nm laser at a temperature of 20K. Figure 4-7 a. shows the macro PL spectrum of the QDs with coverage of 0.63, 0.85, and 1.07 ML of InAs coverage on droplet drilled holes. Emission from the quantum dots have a spectrum with a wavelength that ranges from 820nm to 950nm. Increase in excitation power populates the higher carrier states of the QDs, showing emissions at lower wavelengths. This prove that the emission in this range is from QDs and not from GaAs defects. Emission from the InAs wetting layer, which is observed for self-assembled QDs, is not apparent, confirming that the quantum dots are indeed droplet hole

filled QDs and not self-assembled QDs.

The emission wavelength suggest that an InGaAs QDs have been formed in the holes. During the droplet hole drilling process, residual Ga metal must not have been fully desorbed and remained in the nanohole. This residual Ga metal is assumed to have been mixed with InAs during the formation of the quantum dots. As InAs coverage increases the uniformity of the size of the QDs seem to have increased. The broadening of emission is apparent in lower InAs coverages.

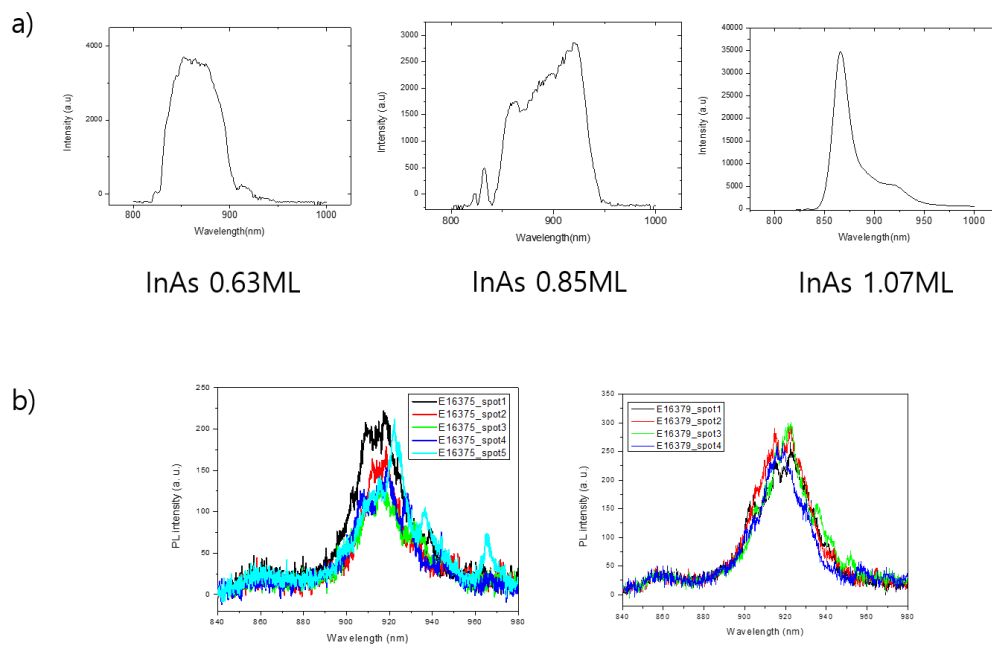


Figure 4-7 a) Macro and b) micro photoluminescence of InGaAs filled nanoholes.

Figure 4-7 b. shows the micro PL at 77K of the 1.07ML sample in figure 4-7 a. The spot size of the laser is about 1 μ m in diameter. Thus, the number of QDs excited is expected to be about 10 to 20 according to the nanohole density from AFM images. This is in good agreement with the micro-PL data. Further analysis to isolate a single quantum dot is needed to measure the emission of a single emitter. A metal layer was deposited with holes to select a few or even an single QD as seen in Figure 4-8.

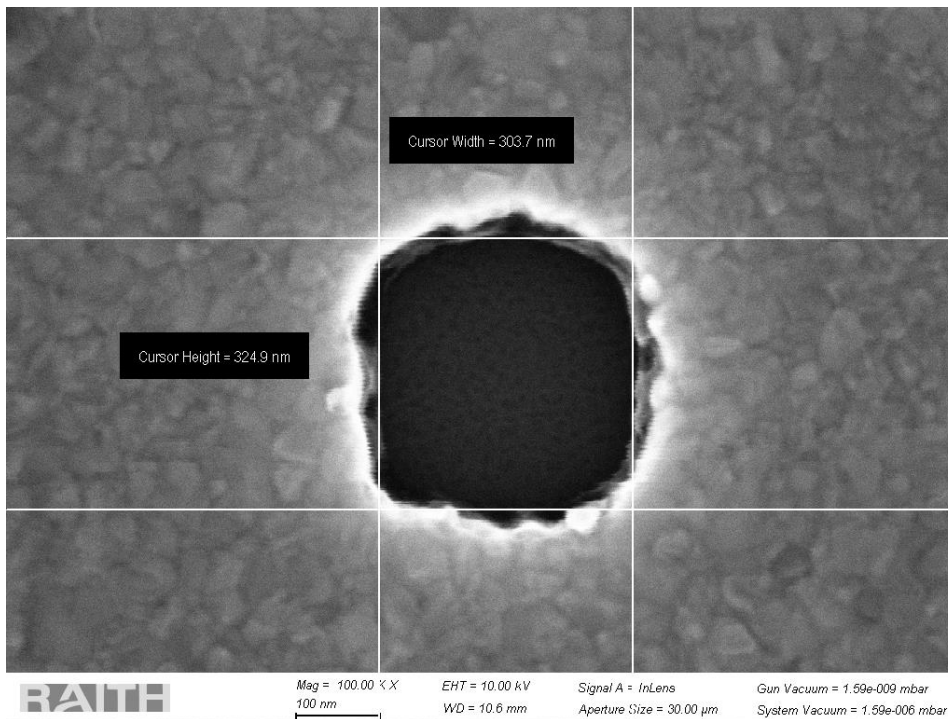


Figure 4-8 SEM image an 100nm thick gold layer with holes deposited on InAs filled hole quantum dot with a GaAs capping layer.

4-3 Symmetry of quantum dots

In the year 2000, O. Benson et al. suggested an entangled photon pair may be generated by exploiting the biexciton cascade in a single quantum dot. [5] The schematic for the process of the biexciton cascade is given in figure 4-9. As discussed in the previous section, the biexciton electrons have spin numbers of $1/2$ and $-1/2$ and the holes have spin numbers of $3/2$ and $-3/2$ in the ground state. The polarization of the photons emitted is determined by the conservation of spin/angular momentum. A total angular momentum of -1 produces a left hand(L) circularly polarized photon while an exciton with a total spin emits a photon polarized in the opposite direction(R).

Two possible decay channels exist for the biexciton. When the $1/2$ electron and $-3/2$ hole recombine first to emit a L polarized photon the exciton left in the QD has a $-1/2$ electron and $3/2$ hole. This exciton subsequently recombines to produce a R photon. On the other hand an R photon could be emitted first with an L photon following. If the two paths of cascade are indistinguishable, the two photon state is described as follows

$$|\Psi\rangle = (|LR\rangle + |RL\rangle)/\sqrt{2}$$

This state expressed in circular polarization basis can also be written with a rectilinear polarization using vertical and horizontal bases or diagonal basis such that

$$|\Psi\rangle = (|LR\rangle + |RL\rangle)/\sqrt{2} = (|HH\rangle + |VV\rangle)/\sqrt{2} = (|DD\rangle + |AA\rangle)/\sqrt{2}$$

Where

$$|H\rangle = (|L\rangle + |R\rangle)/\sqrt{2}, |V\rangle = i(|R\rangle - |L\rangle)/\sqrt{2}$$

and

$$|D\rangle = (|H\rangle + |V\rangle)/\sqrt{2}, |A\rangle = (|H\rangle - |V\rangle)/\sqrt{2}.$$

It can be seen that the state is entangled for three different measurement bases.

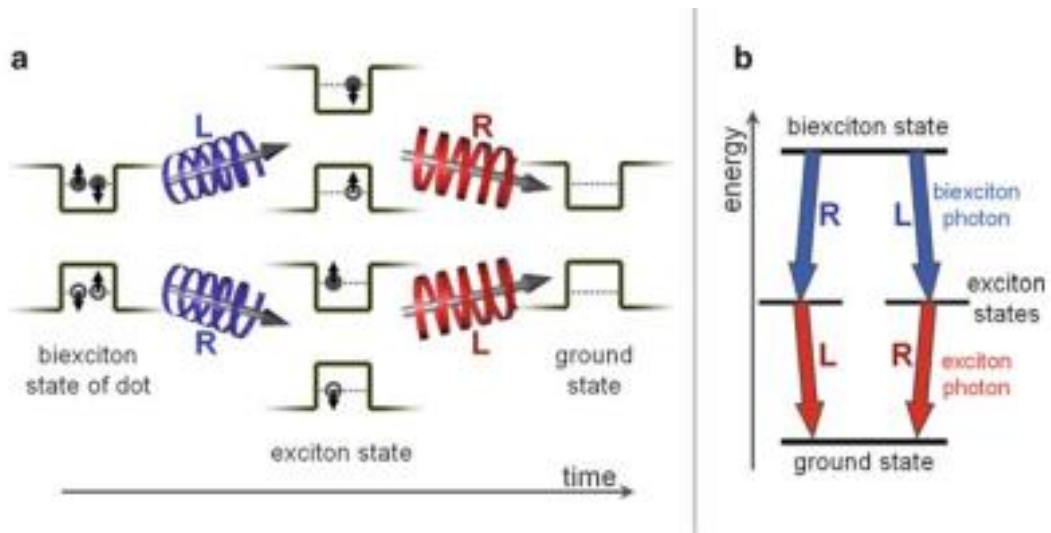


Figure 4-9 a) Schematic of radiative decay process of the biexciton. b) The same two photon emission process in a simple energy level diagram. [1]

The entanglement is destroyed when the energy level splits in the intermediate exciton state. This allows the path of the decay channel to be distinguishable through emitted photon energies. In-plane anisotropy including the shape and strain causes the electron-hole interaction to differ, resulting in a splitting [7,8]. The pure exciton spin state turns into a symmetric and anti-symmetric combinations aligned along axes of the anisotropy. The two exciton states, X_H and X_V couple to biexciton and exciton photon polarized in H and V directions. The fine-structure splitting from this process is shown in figure 4-10.

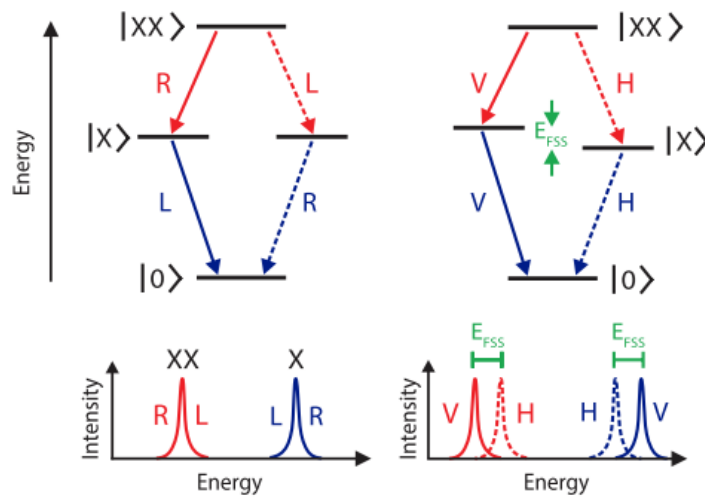


Figure 4-10 Biexciton–exciton cascade for a quantum dot with zero fine-structure splitting (left) and non-zero fine-structure splitting (right). The top row depicts the energy level schemes and below the corresponding emission spectra are depicted. [6]

In order to analyze the anisotropy of the quantum dots, polarization dependence provides information about the electron states inherent to each structure. The measurement of the degree of linear polarization of the PL spectra is defined by

$$P = \frac{I_{[110]} - I_{[1-10]}}{I_{[110]} + I_{[1-10]}}$$

where I is the PL intensity for a given polarization direction.

Optical anisotropy of In(Ga)As self assembled quantum dots have been reported by several research groups [9-13]. Table 4-1 lists the degree of polarization report for InAs and InP quantum dots. The degree of polarization for reported quantum dots range from 7% to 32%. H. Saito et al. have shown in figure 4-11 that the degree of polarization could be measured with macro PL methods [9]. Thus the anisotropy of the quantum dot, which is important in entangled photon experiments is measured by measuring the degree of polarity.

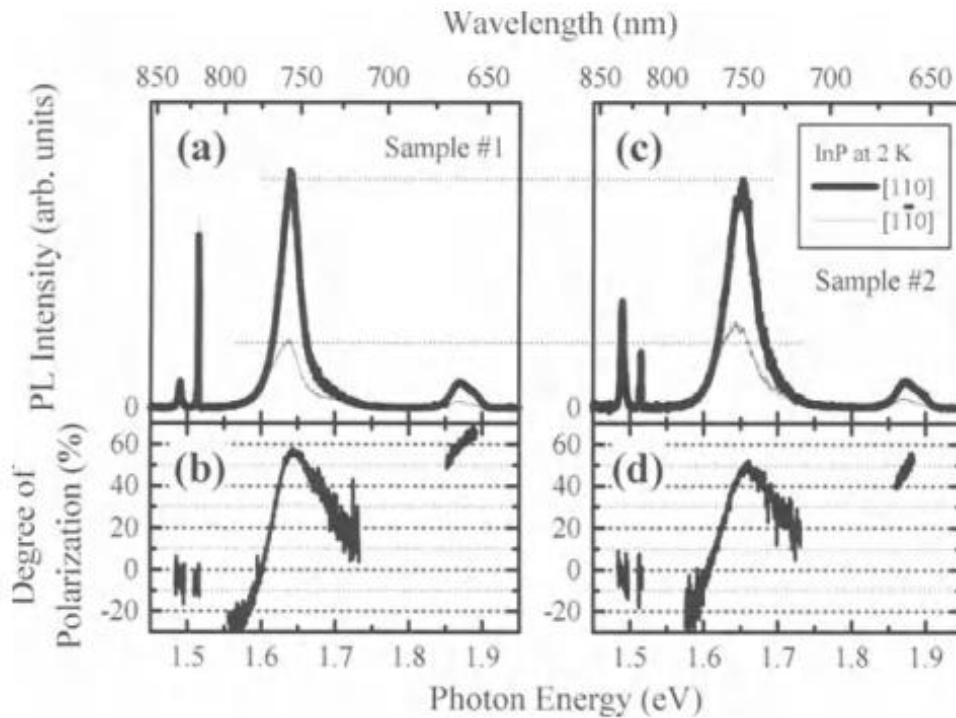


Figure 4-11 (a) Macro-PL spectra at 2 K measured for the [110] (thick curve) and [110] (thin curve) polarizations; (b) Degree of linear polarization of PL spectra shown in (a). The PL band from the GaAs observed at 1.5 eV is isotropic, while those from the InP SADs (1.63 eV) and $\text{Ga}_{0.5}\text{In}_{0.5}\text{P}$ (1.87 eV) show strong optical anisotropy; (c) Polarization dependence of macro-PL spectra measured using another sample with a different degree of matrix ordering. Since the InP SADs layer of sample 2 was grown at the same temperature as that of sample 1, the average dot sizes are the same between the both samples; (d) Degree of polarization of the PL spectra shown in (c) [14]

| Sample | Size of SADs (nm ³) | Aspect Ratio | Degree of polarization in matrix (%) | SADs (%) |
|-----------------------------|------------------------------------|-----------------|---|----------|
| InP (MOVPE #1) ^a | 25 × 35 × 7 | 1.4 | 59 | 55 |
| InP (MOVPE #2) ^a | | | 48 | 44 |
| InP (MBE #1) ^b | 35 × 45 × 6 | 1.3 | 83 | 44 |
| InP (MBE #2) ^b | 40 × 48 × 5 | 1.2 | 30 | 13 |
| InGaAs ^c | 17 × 33 × 3 | 1.9 | | 16 |
| InAs ^d | 13 × 15 × 3 | 1.2 | | 32 |
| InAs ^e | | > 2 | | 13 |
| InAs ^f | 25 × 30 × 3 | 1.2 | | 7 |
| InAs ^g | 16 × 28 × 4 | 1.8 | | 9 |

Table 4-1. Growth temperature, size, aspect ratio, and optical properties of InP SADs in a Ga_{0.5}In_{0.5}P matrix. For comparison, those of In(Ga)As SADs in the GaAs matrix are also summarized [14]

An optical setup for the measurement of polarity is given in figure 4-12. An 800nm femtosecond laser is used to excite the quantum dots at cryogenic temperatures. The emitted photons move through a half wave plate which is rotated to measure the polarity of the photons. Finally, the photons are filtered by a polarizer and measured by an InGaAs photodetector. Sensitivity difference in different axes for the InGaAs detector is the reason a half wave plate rotated instead of the polarizer.

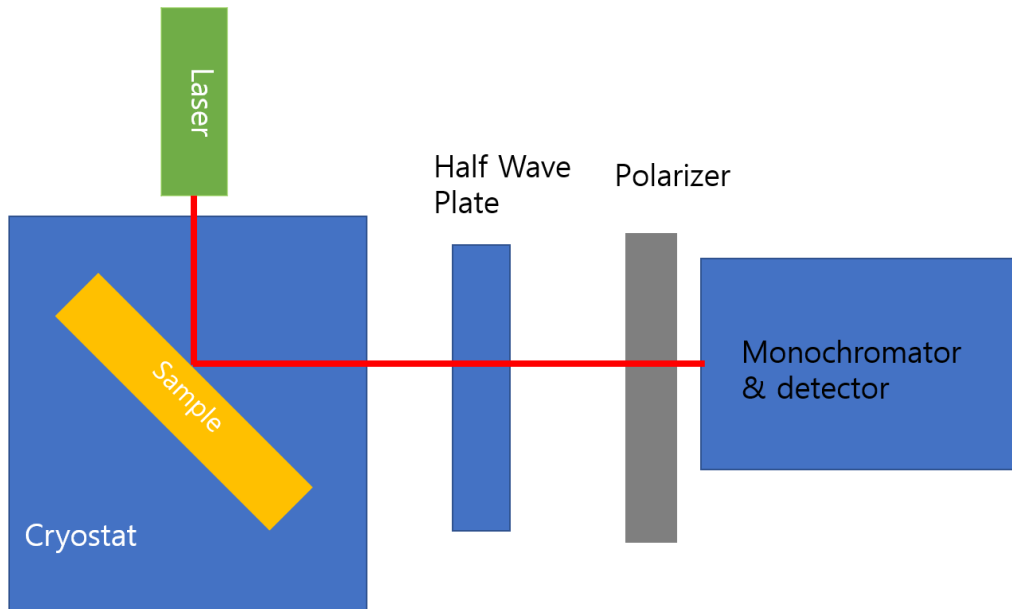


Figure 4-12 Schematic of the optical setup to measure the polarity of quantum dots.

Recent reports have shown that by controlling the polarization dependence fine structure splitting in the quantum dots can be suppressed [15]. This is shown in figure 4-13. Thus by measuring the polarization of the emitted photons, we are able to assess the potential of the quantum dot for the use of entanglement.

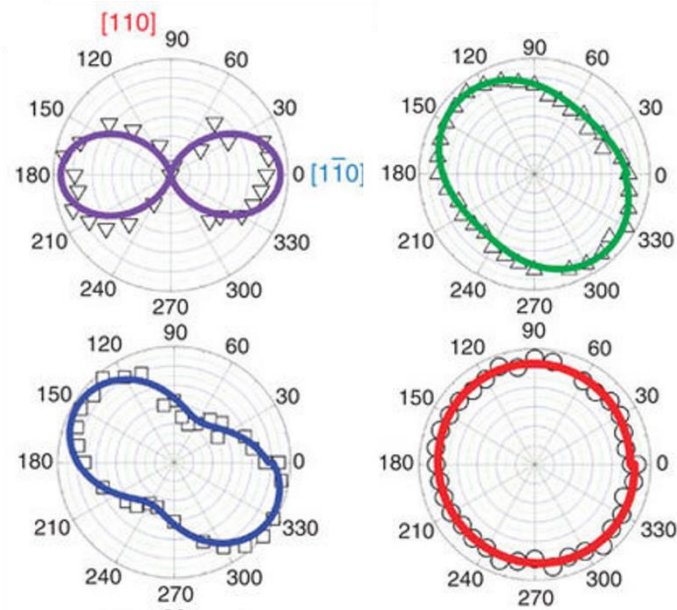


Figure 4-13 Linear polarization dependence of the exciton X at various electric fields [15]

The polarity measurement of the quantum dots fabricated by filling the Ga droplet drilled nanoholes with InAs is shown in figure 4-14. The degree of polarity for each quantum dot sample is 13.4%, 8.17%, 4.02% and 3.33% for samples with InAs coverage of 0.63 ML, 0.85 ML, 1.07 ML and 1.07 ML with a bottom DBR, respectively. It is apparent that as InAs coverage increases, the shape of the quantum dot shows more symmetry. This result combined with the PL result showing high uniformity in the 1.07 ML samples suggest that the shape of the lower part of the hole is not suited well for the growth of ideal quantum dots. This is presumably due to the residual Ga metals not mixing

uniformly with the InAs materials in the lower parts of the hole. On the other hand, the upper parts of the hole show high uniformity and symmetry judging from the PL and degree of polarity.

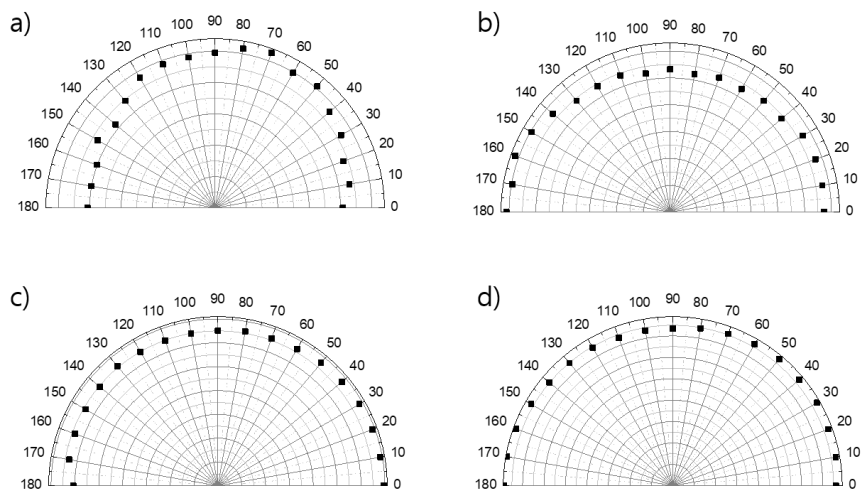


Figure 4-14 Polarization measurement for QDs with InAs coverage of a) 0.63 ML, b) 0.85 ML c) 1.07 ML and d) 1.07ML with DBR.

4-4 Summary

Photoluminescence measurements were conducted on InAs filled nanoholes. The photoluminescence spectra of the quantum dots suggest that the emission is from the QDs that are formed inside the nanoholes and not from other sources. The lack of wetting layer emission and control of excitation intensity confirms this fact. Residual Ga metal from the droplet drilling process makes the emission from the quantum dots to blue shift.

The quantum dots were also tested for polarization. The polarization of the emitted photons give information about the symmetry of the quantum dot. A symmetric quantum dot has the potential to be used as an entangled photon source. The InAs quantum dots in the droplet drilled nanoholes show great symmetry compared to self assembled quantum dots.

Residual Ga metal may have negative effects on the uniformity and symmetry of the quantum dots formed inside the nanoholes.

References

- [1] P. Michler, *Single Semiconductor Quantum Dots*, Springer-Verlag, Berlin (2009)
- [2] T.R. Nielsen, P. Gartner, F. Jahnke, *Phys. Rev. B* 69, 235314 (2004)
- [3] J. Seebeck, T.R. Nielsen, P. Gartner, F. Jahnke, *Phys. Rev. B* 71, 125327 (2005)
- [4] V.D. Kulakowski, B. Bacher, R. Weigand, T. Kummel, A. Forchel, E. Borovitskaya, K. Leonardi, D. Hommel, *Phys. Rev. Lett.* 82, 1780 (1999)
- [5] O. Benson, C. Santori, M. Pelton, T. Yamamoto, *Phys. Rev. Lett.* 84, 2513 (2000)
- [6] A. Orioux, M. Versteegh, K. Jöns and S Ducci, *Rep. Prog. Phys.* 80 (2017) 076001
- [7] V.D. Kulakovskii, G. Bacher, R. Weigand, T. Kmmell, A. Forchel, E. Borovitskaya, K. Leonardi, D. Hommel, *Phys. Rev. Lett.* 82, 1780 (1999)
- [8] O. Stier, M. Grundmann, D. Bimberg, *Phys. Rev. B* 59, 005688 (1999)
- [9] H. Saito, K Nishi, S. Sugou, Y. Sugimoto: *Appl. Phys. Lett.* 71, 590 (1997)4 *Micro-Imaging and Single Dot Spectroscopy* 205
- [10] Y. Nabetani, T. Ishikawa, S. Noda, A. Sasaki: *J. Appl. Phys.* 76, 347 (1994)
- [11] M. Henini, S. Sanguinetti, S.C. Fortina, E. Grilli, M. Guzzi, G. Panzarini, L.C. Andreani, M.D. Upward, P. Moriarty, P.H. Beton, L. Eaves: *Phys. Rev. B* 57, R6815 (1998)
- [12] S. Noda, T. Abe, M. Tamura: *Phys. Rev. B* 58, 7181 (1998)

[13] W. Yang, H. Lee, T.J. Johnson, P.C. Sercel, A.G. Norman: Phys. Rev. B 61, 2784 (2000)

[14] Y. Masumoto, T. Takagahara, Semiconductor Quantum Dots , Springer

[15] M. Ghali, K. Ohtani, Y. Ohno and H. Ohno Nat. Comm. 3, 661 (2012)

5. Site controlled quantum dots

5-1 Local oxidation lithography by AFM

Advanced optoelectronic devices and new applications in nanoelectronics, such as quantum computers require quantum dots to be in an ordered and precisely situated manner. Many different approaches have been attempted to artificially place the QD at predefined sites on pre-patterned substrates [1–9]. When pre-patterning the substrates, it is critical for the lithographic process to not introduce dislocations, impurities or other point defects at the QD nucleation site. This degrades the electronic and optical properties of the QD. In order to overcome this problem an AFM local oxidation lithography has been demonstrated. Arrays of InAs QDs were grown on prepatterned GaAs substrates [10-14].

Many attempts to materialize the site-control of the include using the etch facets [15], a simple lithography technique [16], and regrowth of quantum dots over other quantum dots [17]. However, long distance from the surface [15], limited optical quality [16], and limited growth applications [17] suggests improvements may be made for these QDs.

In this section, we follow the footsteps of previous AFM oxidation lithography techniques to combine the methods with droplet epitaxy.

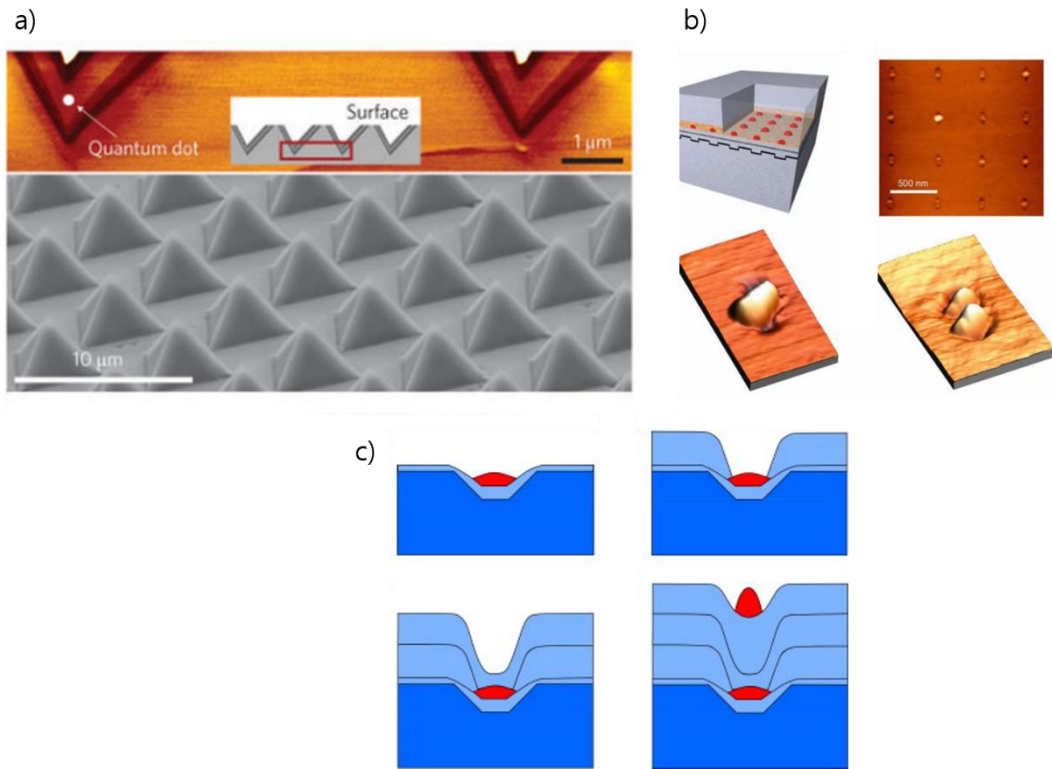


Figure 5-1 Site-controlling methods reported by various groups. a)[15], b)[16], c)[17]

A bias is applied to the AFM cantilever, which creates a localized electric field between the tip and the sample. Since the distance between the tip and the surface of the sample is in the order of a few nanometers, even a moderate tip bias of several volts would generate a field in the range of 100 V/m to 1000 V/m. The extremely high electric field causes field emission, charge injection, Joule heating, electrostatic attraction, explosive

discharge, and electrochemical reactions, which is used to form patterns.

Probe anodic oxidation occurs when the water meniscus at the tip-sample gap is dissociated by the negative tip bias. The resulting O and OH oxidative ions react with the substrate to form localized oxide nanostructures. The oxidized material has a greater molecular volume compared to the substrate which causes the oxidized region to be raised. The oxide states are then etched to produce holes on the substrate. This process is illustrated in figure 5-2.

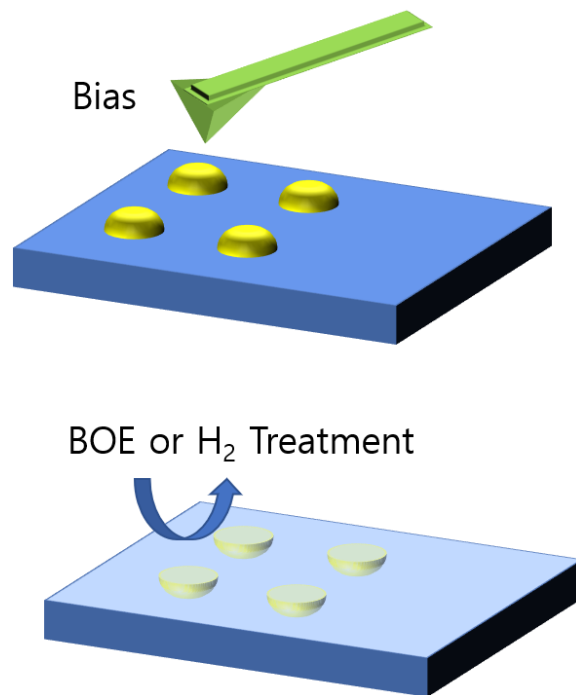


Figure 5-2 Schematic of an anodic oxidation lithography

Several mechanisms have been suggested to explain probe anodic oxidation. Generally, it is accepted that electrical field, surface stress, water meniscus formation, and OH diffusion causes the oxidation [18-29]. The factors which limit the oxidation is not certain among researchers, due to the complexity involved in the nanoscale oxidation.

Avouris et al. confirmed the involvement of ionic species, presumably OH from the water film, in the oxidation by detecting ultra small Faraday currents in situ [20]. According to this report the limitation of the growth rate is from a self-limiting behavior which results from decreasing field strengths and the buildup of stress as the oxide thickness is increased. In this model the rate of oxidation is a function of electric field strength and applied bias, particularly at high fields. Figure 5-3 shows the relationship between the field strength and growth rate of the patterns.

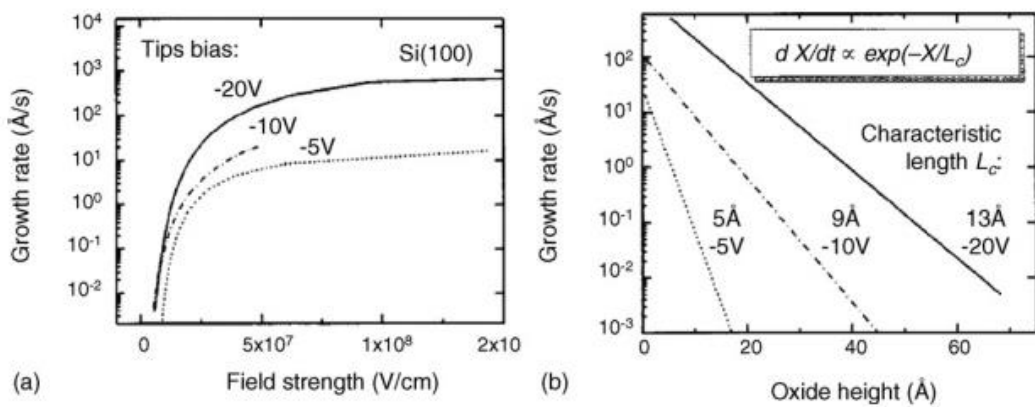


Figure 5-3 a) The growth rate vs. electric field strength. b) Growth rate vs. oxide height at three tip biases [20]

Figure 5-4 shows AFM images oxidation pattern and the etched result for various time exposures to bias. The height of the oxidation mound and the corresponding depth of the etched hole increases with time to a certain point. The limiting factor discussed above appears at around 15 seconds of exposure. However, the diameter of the pattern increases for longer exposures.

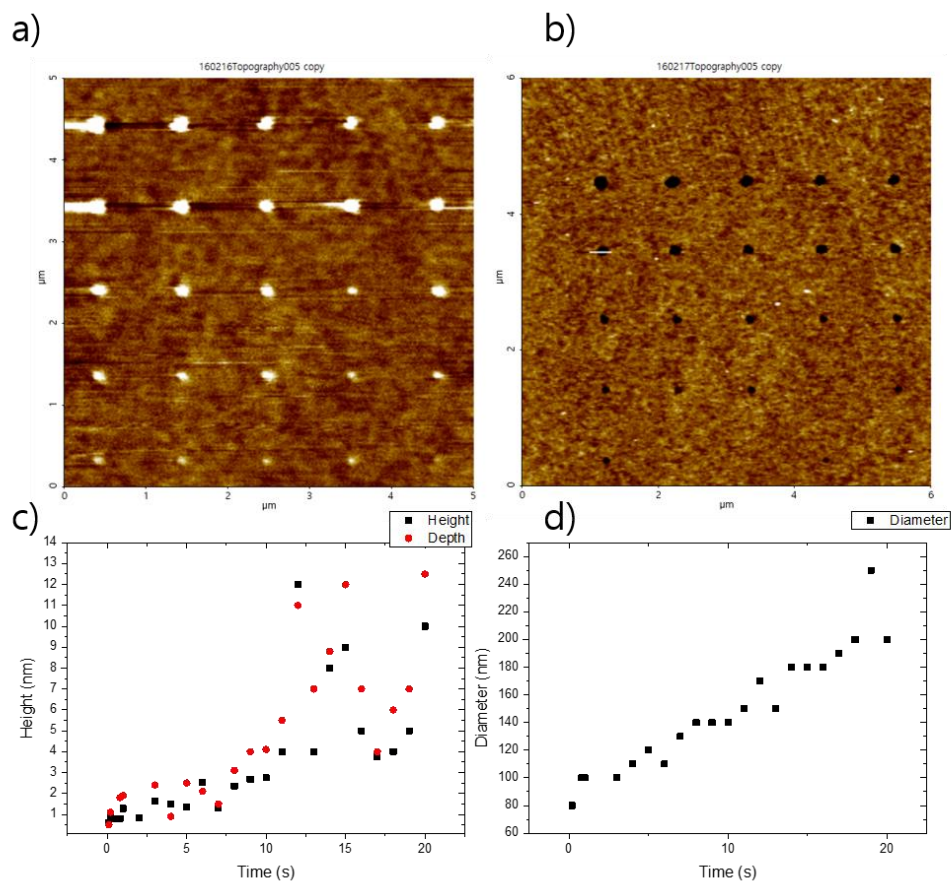


Figure 5-4 AFM image of a) oxidation and b) etched holes. Exposure time dependence of c) height of a) and depth of b) and d) diameter

When the patterned oxides are etched away with either an etchant (HCl or BOE) or hydrogen gas, the oxides that were formed lower than the substrate level are also etched leaving nanoholes. Since the motivation of this work is to achieve symmetry in the shape of quantum dots the shape of the etched holes were also analyzed. Figure 5-5 shows the symmetry of the etched holes. The cross section scan also shows great symmetry.

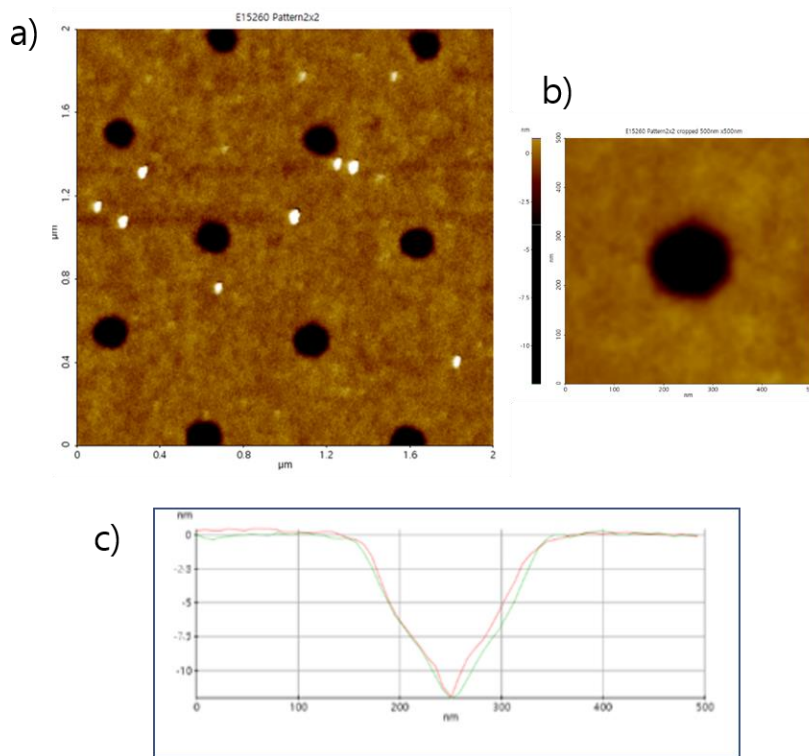


Figure 5-5 AFM image of etched oxide mounds [a,b)] and the cross section scan for perpendicular directions

5-2 Local oxidation etch with droplet drilling

Although local oxidation etch is a promising method for site control of quantum dots, it still is not completely free from exposure to external materials (etchant or hydrogen) during the etching process. Etching a hole with materials native to the quantum dot system is preferable. For this reason, droplet drilling discussed in the previous section is an ideal candidate for the etching process. In this section we attempt to combine the two processes to achieve an ideal patterning method.

Figure 5-6 shows the schematic of the combined process of AFM oxidation and droplet drilling. A substrate is prepared by local oxidation lithography using an AFM and subsequently etched to reveal a nanohole. The etched surface is exposed to an etching agent and may introduce defects in the quantum dots. A droplet drilling step follows where Ga droplets are deposited on the patterned substrate and move toward the patterned hole being trapped. This follows the multistage drilling method introduced in the previous section. The surface movement of the Ga metals allow for the Ga droplets to form only at the etched holes. An annealing process allows the Ga droplets to drill deeper into the patterned holes and away from the etchant exposed surface. This method allows a QD system close to the surface while not being directly in contact with the etched surface.

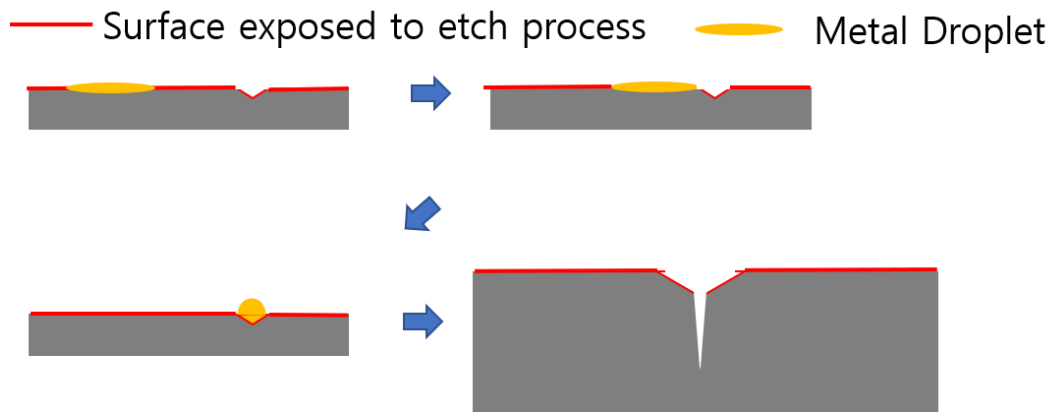


Figure 5-6 Schematic of the local oxidation pattern combined with droplet drilling.

The AFM images from the multistage droplet drilling process is shown in figure 5-7. It is apparent that the droplets find the holes leave no holes unfilled. This result can be exploited to use the method with local oxidation patterning process.

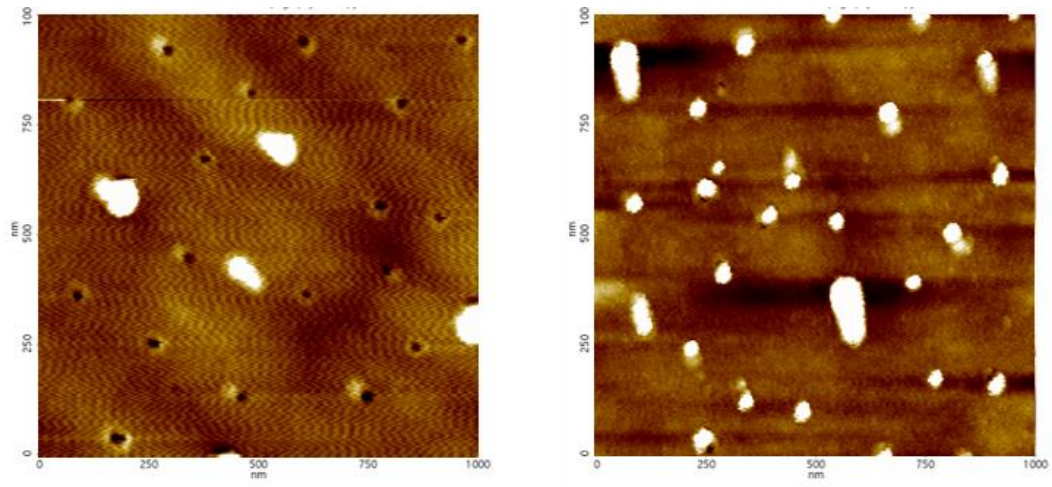


Figure 5-7 AFM images of droplet drilled holes before and after being filled with Ga droplets.

Reference

- [1] B.D. Gerardot, G. Subramanian, S. Minvielle, H. Lee, J.A. Johnson, W.V. Schoenfeld, D. Pine, J.S. Speck, P.M. Petroff, *J. Crystal Growth* 236 (2002) 647.
- [2] X. Mei, D. Kim, H.E. Ruda, Q.X. Guo, *Appl. Phys. Lett.* 81 (2002) 361. ARTICLE IN PRESS
- [3] T. Ohshima, H.Z. Song, Y. Okada, K. Akahane, T. Miyazawa, M. Kawabe, N. Yokoyama, *Phys. Stat. Sol. (c)* 0 (2003) 1364.
- [4] H.Z. Song, Y. Nakata, Y. Okada, T. Miyazawa, T. Ohshima, M. Takatsu, M. Kawabe, N. Yokoyama, *Physica E* 21 (2004) 625.
- [5] S. Kiravittaya, H. Heidemeyer, O.G. Schmidt, *Physica E* 23 (2004) 253.
- [6] Y. Nakamura, N. Ikeda, S. Ohkouchi, Y. Sugimoto, H. Nakamura, K. Asakawa, *Jpn. J. Appl. Phys.* 43 (2004) L362.
- [7] S. Watanabe, E. Pelucchi, B. Dwir, M.H. Baier, K. Leifer, E. Kapon, *Appl. Phys. Lett.* 84 (2004) 2907.
- [8] S. Birudavolu, N. Nuntawong, G. Balakrishnan, Y.C. Xin, S. Huang, S.C. Lee, S.R.J. Brueck, C.P. Hains, D.L. Huffaker, *Appl. Phys. Lett.* 85 (2004) 2337.
- [9] H.Z. Song, T. Usuki, S. Hirose, K. Takemoto, Y. Nakata, N. Yokoyama, Y. Sakuma, *Appl. Phys. Lett.* 86 (2005) 113118

- [10] R. Garcí a, M. Calleja, H. Rohrer, J. Appl. Phys. 86 (1999) 1898.
- [11] Y. Okada, Y. Iuchi, M. Kawabe, J.S. Harris Jr., J. Appl. Phys. 88 (2000) 1136.
- [12] T. Yasuda, S. Yamasaki, S. Gwo, Appl. Phys. Lett. 77 (2000) 3917.
- [13] A. Dorn, M. Sigrist, A. Fuhrer, T. Ihn, T. Heinzel, K. Ensslin, W. Wegscheider, M. Bichler, Appl. Phys. Lett. 80 (2002) 252.
- [14] J.S. Kim, M. Kawabe, N. Koguchi, J. Crystal Growth 262 (2004) 265
- [15] G Juska et al. Nature Photonics 7, 527 (2013)
- [16] S Maier et al. Semicond. Sci. Technol. 29 052001 (2014)
- [17] T.J.Pfau et al. Microelectronic Engineering 87 1357 (2010)
- [18] A.E. Gordon, R.T. Fayfield, D.D. Litfin, T.K. Higman, J. Vac. Sci. Technol. B 13 (1995) 2805.
- [19] D. Stie´venard, P.A. Fontaine, E. Dubois, Appl. Phys. Lett. 70 (1997) 3272.
- [20] Ph. Avouris, T. Hertel, R. Martel, Appl. Phys. Lett. 71 (1997) 285.
- [21] J.A. Dagata, T. Inoue, J. Itoh, H. Yokoyama, Appl. Phys. Lett. 73 (1998) 271.
- [22] J.A. Dagata, T. Inoue, J. Itoh, K. Matsumoto, H. Yokoyama, J. Appl. Phys. 84 (1998) 6891.
- [23] J.A. Dagata, F. Perez-Murano, G. Abadal, K. Morimoto, T. Inoue, J. Itoh, H.

Yokoyama, Appl. Phys. Lett. 76 (2000) 2710.

[24] J.A. Dagata, F. Perez-Murano, C. Martin, H. Kuramochi, H. Yokoyama, J. Appl. Phys. 96 (2004) 2386.

[25] E. Dubois, J.-L. Bubendorff, J. Appl. Phys. 87 (2000) 8148.

[26] E.S. Snow, G.G. Jernigan, P.M. Campbell, Appl. Phys. Lett. 76 (2000) 1782.

[27] H. Jungblut, D. Wille, H.J. Lewerenz, Appl. Phys. Lett. 78 (2001) 168.

[28] R. Garcí a, M. Calleja, H. Rohrer, J. Appl. Phys. 86 (1999) 1898.

[29] J.A. Dagata, F. Perez-Murano, C. Martin, H. Kuramochi, H. Yokoyama, J. Appl. Phys. 96 (2004) 2393.

6. Conclusion

Droplet epitaxy is a versatile technique in the field of nanostructure growth. The separation of group III materials and group V materials has opened up new possibilities in the growth of nanostructures. Many different quantum structures such as quantum dots, quantum rings, quantum holes have been reported to be grown with droplet epitaxy. Throughout this work, we have attempted many different methods using droplet epitaxy to utilize the method to its fullest potential.

Various growth techniques using droplet epitaxy were researched and optimized for quantum dot growth. AFM, TEM, PL characterization techniques were used to characterize the quantum structures grown by droplet epitaxy. Control of density and size of the quantum dots were possible. Quantum dots with thin capping layers were grown using droplet epitaxy. An internal thermal heating process was introduced during the droplet epitaxy growth sequence to achieve high quality quantum dots with a thin capping layer. Such quantum dots may be used for plasmonic applications.

Droplet drilling was used to grow quantum dots with high symmetry in shape. The symmetry of the droplet drilled hole follow the shape of the metal droplets. The nanoholes drilled with Ga droplets are filled with InAs and capped with a GaAs layer to form quantum dots. A multistage drilling method was introduced to overcome the temperature limitation of the annealing process. The symmetry is confirmed with PL measurements. Quantum dots with perfect symmetry show low degree of polarization.

A local oxidation lithography method with an AFM was used to position quantum dots from droplet epitaxy. The AFM lithography methods allow for quantum dot growth with limited exposure to etching agents. Droplet drilling a material native to the QD system that may improve AFM lithography. By combining droplet drilling with AFM lithography, the quantum dots were able to be spatially separated from the etched surface.

국문 요약

금속방울 성장법을 이용한 위치 선정 양자점의 성장과 분석

반도체 양자점은 양자광학 소자의 개발을 위해 많은 연구가 진행되고 있다. 최근에 한 개의 양자점을 이용하여 양자암호나 양자컴퓨터의 개발이 가능하다는 것이 입증되었다. 하지만 실용적인 이를 응용하기 위한 양자소자를 만들기 위해서는 아직도 극복해야한 난제들이 많다. 금속방울 성장법은 양자나노 구조를 성장하기 위한 다목적의 방법이다. 3 족 원소와 5 족원소를 분리함으로써 나노구조 성장에 있어서 새로운 가능성을 열었다. 금속방울 성장법을 이용하면 여태 자기조립 방식의 양자점이 갖고 있는 단점들을 극복하여 단광자 광원과 같은 양자광학 소자들을 만들 수 있다.

이 연구는 금속방울 에피 성장법과 금속방울을 이용한 다양한 성장법들을 이용하여 양자광학 소자를 만들기 위한 기초를 마련하는데 있다. 금속방울 성장법과 다양한 비소화 과정을 실험하였다. 이에 더해 특정한 열화과정을 통해 플라즈모닉스에 이용될 수 있는 얇은 덩개층을 갖고 있는 양자점의 성장에 성공하였다.

금속방울의 여러가지 응용 방법 중에 금속방울을 이용한 식각방법에 대해 실험을 하여 이를 통한 개선된 양자점을 만들었다. 금속방울 식각을 통해 생성된 나노크기의 구멍들은 대칭 양자점을 만들기 위한 기본틀을 마련하였다. 양자점의 대칭은 양자꼬임 현상을 일으키는 광자들을 생성하기 위해 필수적인 요소이다. 이 작은 나노 구멍들은 비화인듐으로 채워져서 비화인듐 양자점을 생성한다. 금속방울 식각시에 나타나는 온도의 한계를 극복하기 위하여 다단계 식각방법을 개발하였다. 이 다단계 식각방법을 원자현미경을 통한 위치 선정법과 병합하여 고품질의 양자점의 위치선정을 할 수 있었다.

List of Publications

[J1] GaAs droplet quantum dots with nanometer-thin capping layer for plasmonic applications - Suk In Park, Oliver Joe Trojak, Eunhye Lee, Jin Dong Song, Jihoon Kyhm, Ilki Han, Jongsu Kim, Gyu-Chul Yi and Luca Sapienza 2018 Nanotechnology 29 205602

[J2] Growth and optical characteristics of high-quality ZnO thin films on graphene layers - Suk In Park, Youngbin Tchoe, Hyeonjun Baek, Jaehyuk Heo, Jerome K. Hyun, Janghyun Jo, Miyoung Kim, Nam-Jung Kim, and Gyu-Chul APL Materials 3, 016103 (2015)

[J3] Metallic nanorings for broadband, enhanced extraction of light from solid-state emitters- Oliver Joe Trojak, Suk In Park, Jin Dong Song, Luca Sapienza. Appl. Phys. Lett. 111, 021109 (2017)

[J4] Indistinguishable and efficient single photons from a quantum dot in a planar nanobeam waveguide - Gabija Kiršanskė, Henri Thyrrestrup, Raphaël S. Daveau, 1Chris L. Dreeßen, Tommaso Pregnolato, Leonardo Midolo, Petru Tighineanu, Søren Stobbe, Rüdiger Schott, Arne Ludwig, Andreas D. Wieck, Suk In Park, Jin D. Song, Andreas V. Kuhlmann, Immo Söllner, Matthias C. Lobl, 4Richard J. Warburton, and Peter Lodahl Phys. Rev. B 96, 165306 (2017)

[J5] Combined metallic nano-rings and solid-immersion lenses for bright emission from single InAs/GaAs quantum dots - Oliver Joe Trojak, Christopher Woodhead, Suk In Park,

Jin Dong Song, Robert James Young, Luca Sapienza. *Appl. Phys. Lett.* accepted

[J6] Deterministic Integration of Quantum Dots into on-Chip Multimode Interference Beamsplitters Using in Situ Electron Beam Lithography - Peter Schnauber, Johannes Schall, Samir Bounouar, Theresa Höhne, Suk-In Park, Geun-Hwan Ryu, Tobias Heindel, Sven Burger, Jin-Dong Song, Sven Rodt, and Stephan Reitzenstein *Nano Lett.* 18, 4, 2336 (2018)

